



Monsoon hysteresis reveals atmospheric memory

Anja Katzenberger^{a,b} and Anders Levermann^{a,b,c,1}

Edited by Hans Schellnhuber, International Institute for Applied Systems Analysis, Laxenburg, Austria; received September 8, 2024; accepted March 6, 2025

Within Earth's climate system, the ocean, cryosphere, and vegetation exhibit hysteresis behavior such that their state depends on their past and not merely on their current boundary conditions. The atmosphere's fast mixing time scales were thought to inhibit the necessary memory effect for such multistability. Here, we show that moisture accumulation within the atmospheric column generates hysteresis in monsoon circulation independent of oceanic heat storage and yields two stable atmospheric states for the same solar insolation. The dynamics of monsoon rainfall is thus that of a seasonal transition between two stable states. The resulting hysteresis is shown in observational data and reproduced in a general circulation model where it increases with decreasing oceanic memory and exhibits the two distinct states that persist for more than 60 y. They are stabilized by moisture accumulation within the atmospheric column that carries information across time scales much longer than those typical for mixing. The possibility of abrupt shifts between these two states has implications for the future evolution of global monsoon rainfall that is crucial for the agricultural productivity currently feeding more than two billion people.

monsoon circulation | atmospheric memory | hysteresis behavior | tipping points | climate change

Hysteresis behavior is found in a number of systems whenever their current state does not merely depend on their current boundary conditions but their history. This nonlinearity represents a stabilizing memory effect and is prevalent across different disciplines ranging from the physics of ferromagnets (1) to the economics of unemployment (2). Hysteresis, in the narrow sense, as it is used here, is not merely a delayed response of a system to external forcing due to inertia within the system (which could be denoted hysteresis in the wider sense or rate-dependent hysteresis), but has two underlying stable steady states for the same boundary condition. The system's memory is required in order to stabilize the system's state against fluctuations in the external forcing or internal variability. Thus the time scale of the memory decay has to be significantly longer than typical fluctuations within the system or in the external forcing. The hysteresis then becomes an equilibrium or rate-independent hysteresis.

In the Earth system, hysteresis has been found in the context of increasing and decreasing atmospheric CO₂ concentrations (e.g. refs. 3–5) and may be associated with abrupt transitions of a system between two qualitatively different states. Greenland, for example, can either carry an ice sheet or be ice-free, for the same global climatic boundary conditions. The reason is that a massive ice sheet reaches high up into the atmosphere where it is colder than at sea level which then allows the ice sheet to be sustained even if it would not form under the same global climate conditions (6). Another paleoclimatic example is made possible by the ice-albedo feedback, that determines whether for a given solar radiation the Earth stabilizes in a warm state or in the so-called snowball Earth state (7–9). Central to this behavior is a long time scale that can carry the memory within the system across typical time scales of changes in the external forcing and the internal variability and thereby stabilize the two distinct states. Consequently, hysteresis has so far been found in the ocean, the vegetation, and the cryosphere—specifically in the Antarctic and Greenland Ice Sheets (10, 11), the Atlantic Meridional Overturning Circulation (12–14), the El Niño-Southern Oscillation (15), the upper ocean heat content, acidification, and thermohaline sea level rise (16–18) as well as tropical rainforests (19). The combination of two oceanic memory effects, namely in the Atlantic overturning and in the slower warming or cooling in the Southern Ocean, could yield hysteresis in the Inter-Tropical Convergence Zone (20) or mid-latitude storm tracks (21). The accumulation of heat in the ocean has been shown to cause hysteresis of global mean precipitation (22) as well as the asymmetry of monsoon systems in a CO₂ ramp-up and ramp-down in numerical simulations, and El-Niño-related anomalies (4, 5, 23). In some of these systems, it is not yet clear whether the system exhibits hysteresis only in a wider sense, i.e., shows merely an inert response to the change in

Significance

Monsoon circulations are crucial for the livelihood of more than two billion people on Earth. Here, we show that the underlying dynamics that causes the monsoon rainfall is that of a seasonal transition between two stable states. Each year, the system flips from an “off state” in winter to an “on state” in summer and back. The stability of these states reveals an atmospheric memory that is longer than previously thought possible. As a consequence, monsoon circulations can abruptly switch on and off if climatic boundary conditions change. Whether this places current monsoon systems at danger of abrupt cessation needs to be investigated in future studies.

Author affiliations: ^aPotsdam Institute for Climate Impact Research, Potsdam, 14473 Germany; ^bInstitute for Physics and Astronomy, Potsdam University, Potsdam, 14476 Germany; and ^cLamont-Doherty Earth Observatory, Columbia University, New York, NY 10964-1000

Author contributions: A.L. and A.K. designed research; A.L. designed the conceptual model; A.K. performed research; A.K. and A.L. analyzed data; and A.K. and A.L. wrote the paper.

The authors declare no competing interest.

This article is a PNAS Direct Submission.

Copyright © 2025 the Author(s). Published by PNAS. This article is distributed under [Creative Commons Attribution-NonCommercial-NoDerivatives License 4.0 \(CC BY-NC-ND\)](https://creativecommons.org/licenses/by-nc-nd/4.0/).

Although PNAS asks authors to adhere to United Nations naming conventions for maps (<https://www.un.org/geospatial/mapsgeo>), our policy is to publish maps as provided by the authors.

¹To whom correspondence may be addressed. Email: anders.levermann@pik-potsdam.de.

This article contains supporting information online at <https://www.pnas.org/lookup/suppl/doi:10.1073/pnas.2418093122/-DCSupplemental>.

Published May 6, 2025.

external forcing, but no steady-state bistability. So far atmospheric hysteresis has always originated from an oceanic memory effect (3). The monsoon hysteresis in this study, however, does not rely on oceanic memory, but reveals a memory effect within the atmosphere itself. This possibility was first suggested in a conceptual model (24), but it has never been shown in a three-dimensional model.

Seasonal Hysteresis of Observed Regional Monsoon Rainfall

The central characteristic of monsoon rainfall is the seasonal reversal of winds by at least 120° associated with qualitatively different states of humidity, cloudiness, and rainfall (25, 26). This annual cycle of precipitation is driven by the oscillating incoming insolation as revealed, for example, by empirical orthogonal function analysis (27). Thus, the oscillating solar radiation is the responsible forcing for shaping the seasonal character of monsoon rainfall and provides the upper atmospheric boundary condition for the system. When monsoon rainfall in different parts of the world is considered as a function of this planetary boundary condition, observations (Fig. 1) show that rainfall intensifies in spring at much higher solar insolation than it decreases in autumn. In Central India (17 to 26°N , 76 to 82°E), for example, the same insolation of approx. 435 W/m^2 is associated with two

very different rainfall regimes: a state of no rainfall in April and abundant precipitation in August. We choose central India as an example of a land monsoon for later comparing it to the land monsoon of the Monsoon Planet. However, the bistability sustains also for larger regions over India; see *SI Appendix, Fig. S1*. The hysteresis behavior is also present in other monsoon system as e.g. over the Bay of Bengal, East Asia, and Australia (Fig. 1 *D–F*), as well as West African, North American, and South American Monsoon (*SI Appendix, Fig. S3*).

Since the extraterrestrial forcing of the region is the same for both states, the different rainfall regimes must be originating from a memory within the Earth system itself. Natural candidates for this memory are the land surface including vegetation or the ocean. The rainfall shows the same hysteresis behavior when it is plotted over the land surface temperature as the lower boundary condition of the atmospheric column (*SI Appendix, Fig. S5*) and the surface albedo only differs marginally between the two states which rules out the land surface as a carrier of the memory.

Seasonal Hysteresis on the Monsoon Planet

To investigate the role of the ocean in carrying the memory of the monsoon system we reproduce the general characteristics of the observed monsoon hysteresis in the GFDL-AM2 atmospheric general circulation model, developed by the Geophysical Fluid

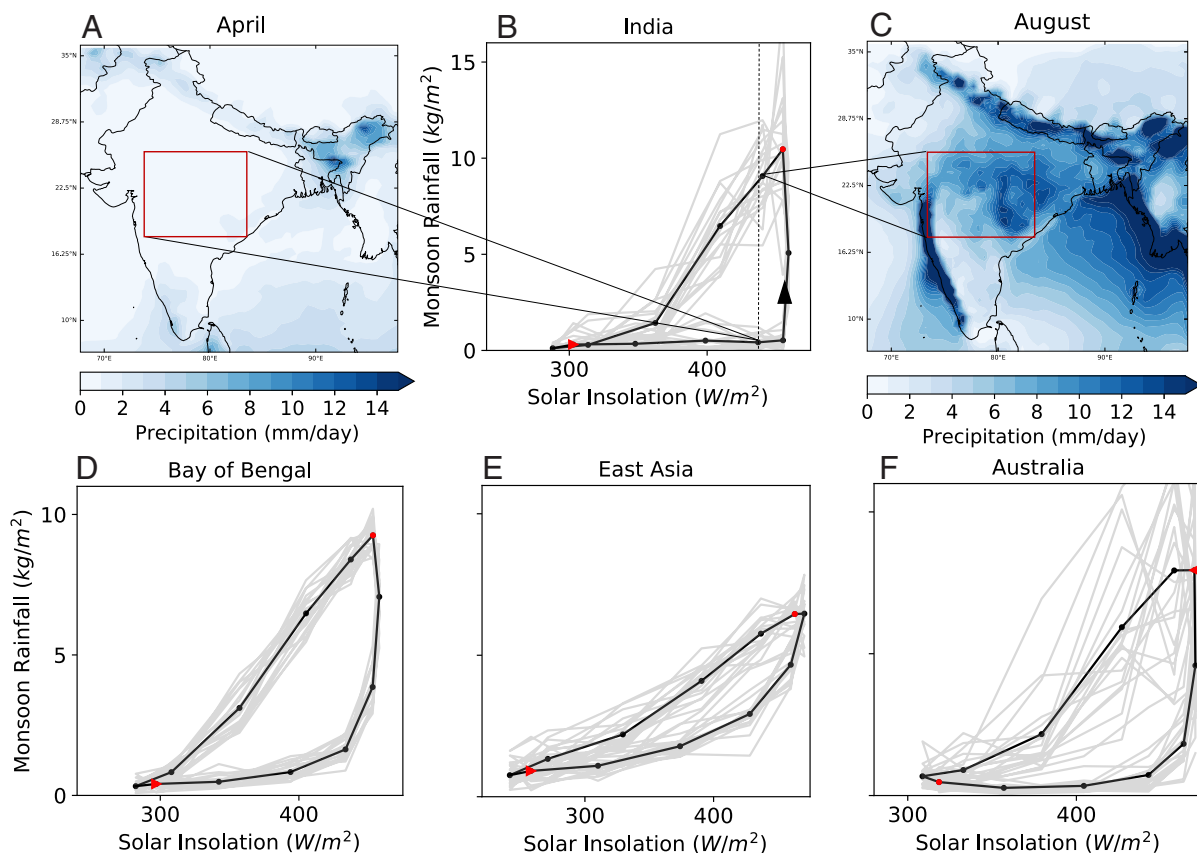


Fig. 1. Observed seasonal monsoon hysteresis for Central India panels (A–C) and other monsoon regions panels (D–F). Panel (B) shows the monthly observed rainfall data for a land region of central India (17 to 26°N , 76 to 82°E) as a function of the associated solar insolation. (The results sustain also for a larger region over India; see *SI Appendix, Fig. S1*.) The gray lines show the results for individual years, the 20-y average is shown in black yielding a seasonal monsoon hysteresis. The red triangle (circle) marks December (July) and the progression of the year follows the direction indicated by the triangle symbol. The vertical dashed line marks two moments with the same solar insolation that are associated with two rainfall states: In April there is no relevant rainfall over the monsoon region (A), while in August there is monsoon rainfall (C). (More details regarding the annual development of the key climate variables for the Indian monsoon is presented in *SI Appendix, Fig. S2*.) The panels (D–F) show the seasonal hysteresis for the Bay of Bengal, East Asia, and Australia. Further monsoon systems (West African, North American, and South American Monsoon) are shown in *SI Appendix, Fig. S3*. The underlying regions are shown in *SI Appendix, Fig. S4*. Data sources: CERES for solar insolation, GPCC for rainfall; see *SI Appendix*.

Dynamics Laboratory (GFDL) (28). In order to generate a generic monsoon system, we apply a simplified representation of continents, specifically an “aquaplanet” with a circumglobal land stripe extending from 10 to 60°N (*SI Appendix, Fig. S6*). The seasonal rainfall distribution in this idealized simulation reproduces the meridional monsoon circulation (*SI Appendix, Fig. S8*) and fulfills the general definition of monsoon rainfall (29–31). The monsoon region is located just equatorward of the peak in the subcloud moist static energy (32–36) and poleward from a barrier in the surface pressure (36). The surface temperature different between the sea surface and the land surface is largest right before the monsoon onset (*SI Appendix, Fig. S9*) as it was found earlier for the Indian monsoon (37). It then declines due to the cooling effect of the rainfall on the land surface. Further details regarding the monsoon dynamics are provided in *Monsoon on the Monsoon Planet* and can be found in a published sensitivity analysis with the same model set-up (36). In *SI Appendix, Figs. S10–S13*, we present further simulations that show that the hysteresis is robust with regard to changes in solar radiation, sulfate aerosol concentration, land surface albedo, and carbon dioxide concentration and discuss their effects on the hysteresis in *Robustness of Seasonal Hysteresis*. The effect of

increasing carbon dioxide concentration in the atmosphere is of particular relevance, as it indicates how the hysteresis may be altered in the context of climate change during the 21st century. As the water vapor content in the warmer atmosphere increases, the hysteresis effect amplifies. Per degree of global warming, the height of the hysteresis increases: The height of the hysteresis concerning moisture content increases by approx. 9.5% per degree of global warming, resulting in an increase of the hysteresis height regarding monsoon rainfall by 9.5% (*SI Appendix, Fig. S14*). In *SI Appendix, Fig. S11*, we provide further insights into this relationship based on simulations with 140 ppm, 280 ppm, 400 ppm, and 560 ppm atmospheric CO₂ concentration.

The Monsoon Planet reproduces the hysteresis behavior of the observations (Fig. 2A), i.e. the same extraterrestrial boundary conditions in the region 10 to 20°N (*SI Appendix, Fig. S7*) lead to very different rainfall distributions: Taking e.g. the two days when the solar insolation equals 426 W/m² at 15°N, there is no monsoon rainfall on April 3rd, while there is abundant rainfall over the monsoon region on September 1st (*SI Appendix, Fig. S15*). The same hysteresis behavior is found for the lower local boundary conditions (*SI Appendix, Fig. S16*): a surface temperature of, for example, 36 °C can be associated with a

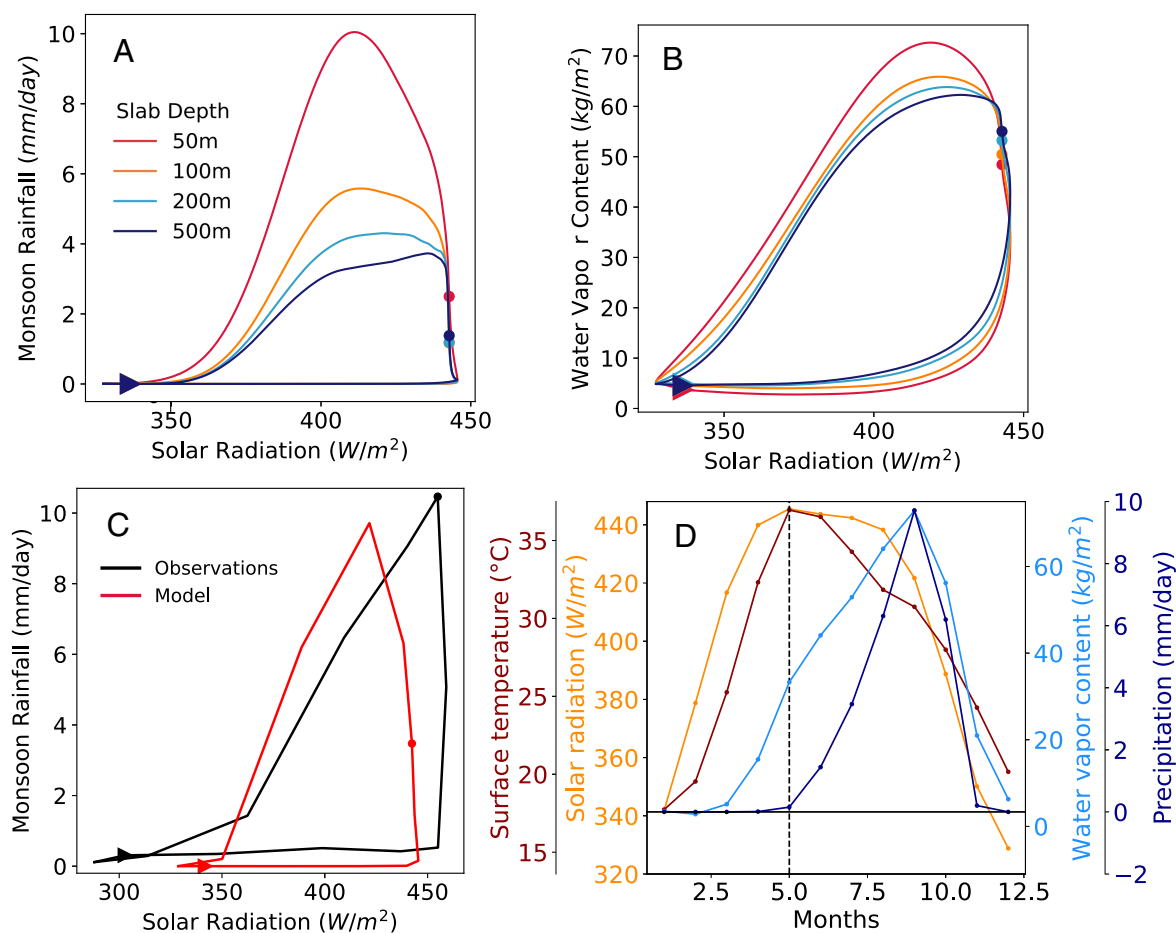


Fig. 2. (A and B) Seasonal Monsoon Hysteresis in the idealized conditions of the Monsoon Planet. Monsoon Rainfall (A) and water vapor content (B) depending on upper boundary conditions (solar radiation). The results are shown for different slab depths (50 m, 100 m, 200 m, and 500 m) simulating different ocean heat capacities. The hysteresis increases when the ocean memory is reduced indicating a memory effect within the atmosphere. The 10-y daily averages smoothed by a Singular Spectrum Analysis method is displayed. The triangle symbol marks January and the direction of the progression of the year, the circle marks July. (C) Comparison of the seasonal hysteresis in the model and observations. Monsoon rainfall depending on the upper boundary conditions in observations over central India (black; GPCC rainfall data combined with CERES data) and the idealized model of the Monsoon Planet with a slab depth of 50 m (red). Markers as in panels (A and B). (D) General characteristics for the Monsoon Planet throughout the year. Results are shown for the monsoon region (10 to 20°N) and for a slab depth of 50 m. The 20-y monthly averages are shown. The vertical dashed line marks May when surface temperature peaks and monsoon rainfall sets on.

state of no rainfall on May 9th as well as strong rainfall on September 1st (*SI Appendix*, Fig. S15). A three-dimensional plot (*SI Appendix*, Fig. S17) and an interactive figure in *SI Appendix* shows for different slab depths that the hysteresis does not collapse when upper and lower local boundary conditions are combined. Thus, as for the observations, the remaining natural candidate for the memory effect would be the ocean. In contrast to the observational data, the model allows to control the oceanic heat capacity by employing a simplified “slab-type” model with varying depths for the mixed layer, ranging from 50 to 500 m. *SI Appendix*, Figs. S18–S22 give an overview of the general climate characteristics of simulations with the different slab ocean depths. When the slab ocean depth and thereby the associated heat capacity of the ocean is reduced (from 500 m, 200 m, 100 m, to 50 m), the hysteresis increases (Fig. 2A) as measured by the area of the loop formed by the trajectory (3) or the difference between the maximum and the minimum for a given insolation. This means that the hysteresis effect becomes stronger when the ocean memory is reduced—excluding oceanic memory as the main cause of the hysteresis.

Atmospheric Memory and Bistability

Instead the memory originates from the accumulation of atmospheric water vapor during the monsoon season (Fig. 2B and *SI Appendix*, Fig. S16 as function of surface temperature).

Water vapor is drawn via the mainly ageostrophic winds from the ocean and accumulates in the atmospheric column (Fig. 2D). When this atmospheric water vapor reservoir exceeds a filling level of approx. 35 kg/m^2 , rainfall onsets (exceeding 0.2 mm/d , Fig. 3 and *SI Appendix*, Figs. S23 and S24). The associated condensation releases latent heat which has been shown to cause small-scale eddy motion within the atmospheric column (32). The associated turbulent kinetic energy is then cascaded down the Richardson cascade into small-scale molecular motion and is thereby heating the atmospheric column (38). The increased molecular motion leads to more collisions, more repulsion between the molecules and a reduction of local pressure. The resulting low pressure system draws winds from the ocean, fueling the existing circulation (39–41). Although these processes are partially parameterized in an atmospheric general circulation model (28), the essence of the real world processes is captured by the GFDL model.

The water vapor that is stored in the atmospheric column is stabilizing the dynamics against synoptic mixing. The typical time scale for synoptic variability is hours to days (39). By contrast the export time scale for the water vapor within the atmospheric column during the monsoon season is of the order of weeks. In order to estimate this memory time scale of the water vapor within the atmospheric column during the rainy period, simulations were carried out in which the solar insolation was switched abruptly to the region’s minimal value (327.8 W/m^2 , reached in

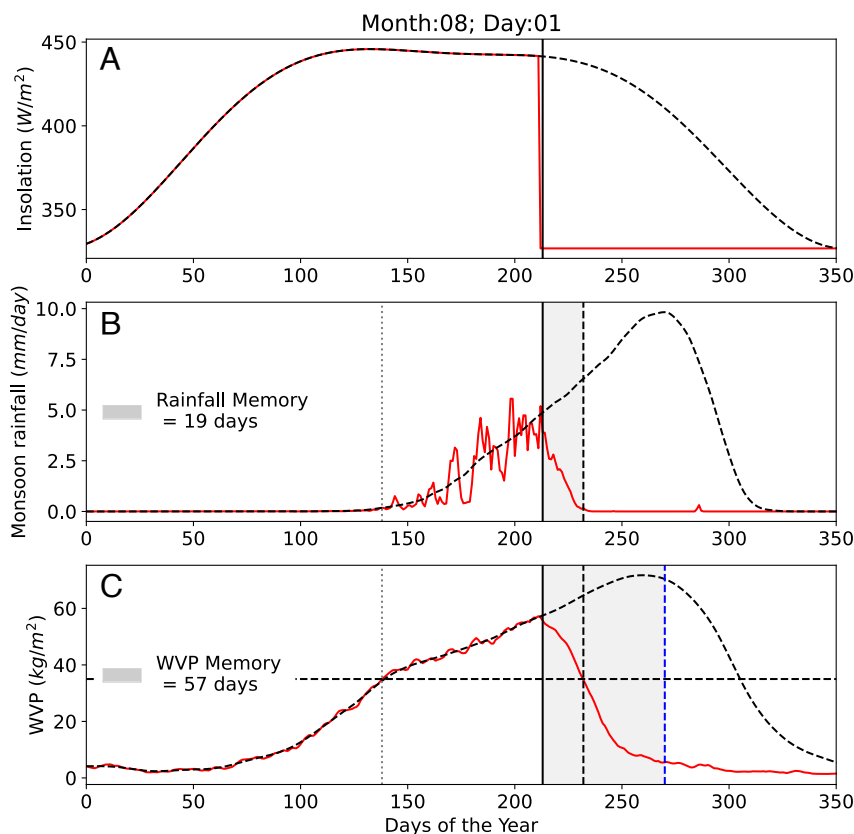


Fig. 3. Quantification of the memory effect for August 1st. The dashed plots indicate the natural course of variables throughout the year, the red plot shows the simulations adapted to study the memory effect. The vertical black line marks the time step of intervention. Panel (A): Insolation in 10 to 20°N develops naturally until August 1st when we abruptly set the radiation to the regional minimum level of 327.8 W/m^2 (usually reached on December 21st). Panel (B): There is no monsoon rainfall before its onset at the beginning of the season (pointed gray vertical line). The rainfall lasts until the timestep marked with a black dashed vertical line. Panel (C): The water vapor (WVP) increases earlier than the rainfall and reaches a threshold of 35 kg/m^2 (black horizontal dashed line) at the timestep marked with a pointed gray vertical line. The blue dashed line marks the day when water vapor falls below 5 kg/m^2 . The memory time span marks the time period that the rainfall (B) and moisture content (C) sustains after interruption of solar radiation by a gray background.

winter, Dec 21st) at different points during the simulation (Fig. 3 and *SI Appendix, Figs. S23 and S24*). The water vapor content then declines to practically zero. The time period of the decline depends on the amount of water vapor that was accumulated and thereby the day within the season at which the insolation was changed. If the switch occurs on Aug 1st, the decay time scale of the water vapor is 57 d (19 d for rain). For a switch-off on Sep 1st, this value reaches 58 d (20 d for rain) and remains similar for Oct 1st at 66 d (15 d for rain). The precise numbers are subject to uncertainty as can be seen from the figures. They are presented here as an estimate of the order of magnitude that is also consistent with the amount of water vapor and its transport by winds and mixing. Independent of the switch date, rainfall stops when water vapor levels fall below 35 kg/m^2 (Fig. 3 and *SI Appendix, Figs. S23–S25*).

As a consequence of this memory, the global atmosphere shows two stable states under the same boundary conditions in the region. Keeping the solar insolation constant at, for example, 427 W/m^2 in spring (Mar 25th) coming out of the winter yields a stable global condition without monsoon rainfall (blue plot in Fig. 4) that remains below 1 mm/d of rainfall for more than 9 mo (A). It then stabilizes after 5 y at a level of about 5 mm/d (B) where it remains stable for the rest of the simulation (C). This state is qualitatively distinct from the situation when the solar insolation is kept at the same value but coming out of the rainy season (Sep 9th). In this case, the rainfall stays well above 6 mm/d for the initial 9 mo and then stabilizes at a level double of the blue curve at 10 mm/d (red lines in Fig. 4). These two states remain stable for the entire simulation time of 60 y. A five-member ensemble of equivalent simulations with different initial conditions shows the robustness of the bistability (Fig. 4 and *SI Appendix, Fig. S27* for individual ensemble members with the original time resolution).

Discussion and Conclusion

The monsoon hysteresis and its associated bistability in this study reveal an atmospheric memory that sustains monsoon circulations: The atmospheric column acts as a reservoir for water

vapor that is filled from February onward. As soon as a threshold of approx. 35 kg/m^2 is reached, the rainfall onset occurs (defined as exceeding 1 mm/d) and sustains the circulation by latent heat release. During the active season, rainfall scales linearly with the amount of accumulated water vapor. When the solar radiation as the external forcing is reduced to its annual minimum in the region, the reservoir stabilizes the rainfall until the reservoir level falls below the threshold of approx. 35 kg/m^2 . This threshold dynamics is consistent with reanalysis data from the Indian Monsoon. But the approximate threshold is lower (daily data: approx. 29 kg/m^2 ; see *SI Appendix, Fig. S28*; monthly data: approx. 22 kg/m^2 ; see *SI Appendix, Fig. S29* in comparison with ref. 42). The resulting memory of precipitation is of the order of several weeks (in our simulations between 8 and 10 wk) exceeding the memory of convection that was quantified to be hours to days and synoptic scale variability (43).

As a result, similar to the Greenland ice sheet which is too massive to be melted down in one summer, the atmospheric moisture accumulation during the rainy season in India prevents small-scale weather systems including dry spills to extinguish the monsoon system between July and September. The end of the rainy season occurs when the solar insolation is so weak that the relative cooling that is generated by the approaching winter is stronger than the latent heating from the condensation (Fig. 2D).

While the model setup with simplified topography and an atmospheric general circulation model coupled to a slab ocean enables us to isolate and systematically study the memory effect, it also has the disadvantage that it limits the transferability of the findings to the real world. In order to bridge this gap between the idealized Monsoon Planet setup to a more realistic representation of the real world, we replaced the oceanic model component with the oceanic general circulation model, MOM-5, and introduced a realistic topography. While computational constraints inhibit a full investigation of the bistability, we find the monsoon hysteresis unchanged (*SI Appendix, Fig. S30*) and thereby consistent with both the observations and the idealized simulations.

In conclusion, our simulations strongly suggest that monsoon systems undergo abrupt transitions tipping points between two

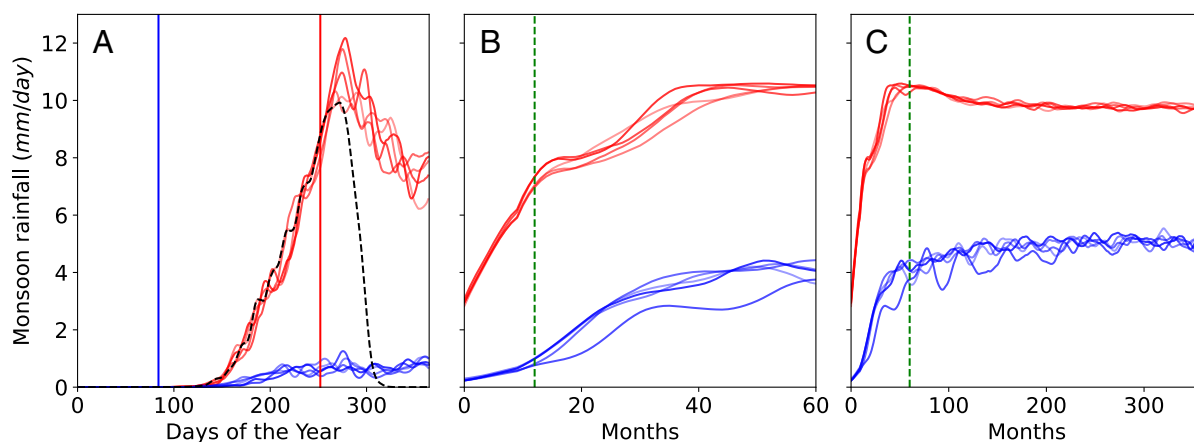


Fig. 4. Bistability of monsoon rainfall: Two stable states for 427 W/m^2 depending on the previous conditions of the system are possible. The state coming from winter conditions is shown in blue, the state starting in summer in red. We perform simulations in which the solar insolation develops naturally until 25th March (vertical blue line) when 427 W/m^2 is reached in the monsoon region (10 to 20°N). After this date, we keep solar radiation constant at 427 W/m^2 (blue). In another set of simulations, we let the radiation develop until 427 W/m^2 on 9th September (vertical red line) and keep it constant afterward (red). See *SI Appendix, Fig. S26* for an illustration of the procedure. The black dashed plot in panel (A) marks the undisturbed rainfall throughout the year. Depending on the previous state, two equilibrium states are possible for monsoon rainfall as shown in Panels (A–C) for different time periods: Panel (A) shows daily data for the first year, panel (B) shows the monthly averages of these simulations continued with the solar radiation of 427 W/m^2 over a period of 60 mo and panel (C) over 350 mo. The time series have been smoothed by singular spectrum analysis with a window size of 10 d (A) and 10 mo (B and C). The vertical dashed green lines in panel (B) (panel C) mark the end of the time window shown in panel (A) (panel B). An ensemble of five simulations with varying initial conditions are shown. The individual ensemble members in model resolution are presented in *SI Appendix, Fig. S27*.

stable states every year. These transitions are forced by the varying solar insolation. The observed hysteresis (Fig. 1) is thus not an inert response of a monostable system but is the expression of an underlying bistability. In contrast to other systems such as the Greenland or Antarctic ice sheets, the threshold for monsoon systems can thus be analyzed using observational data, since it is being crossed annually. This yields the possibility that a change in environmental conditions, such as a further increase in atmospheric greenhouse gas concentrations or aerosol loading of the atmosphere, may push monsoon system across a dynamical tipping point (44) and, potentially leading to the cessation of existing monsoon systems or the onset of new ones.

Methods

Climate Data. We use data from the Clouds and the Earth's Radiant Energy System (CERES) Energy Balanced and Filled top-of-atmosphere, Edition 4.2 project whose instruments fly on the Terra, Aqua, Suomi National Polar-Orbiting Partnership, and NOAA-20 satellites (45) with $1^\circ \times 1^\circ$ monthly resolution for incoming solar radiation. One of the central goals of CERES is to produce a long-term, integrated global climate data record for detecting decadal changes in the Earth radiation budget from the surface to the Top of Atmosphere together with the associated cloud and aerosol properties (45). In addition, we use monthly $1^\circ \times 1^\circ$ rainfall data from the Global Precipitation Climatology Centre (GPCC) (46). The data are based on approx. 86,000 stations world-wide that feature record duration of 10 y or longer. For surface temperature, we use monthly land surface temperature from MODIS (Moderate resolution Infra-red Spectroradiometer) on Terra, level 3 collated (L3C) global product (2000–2018), version 3.0 from the European Space Agency Climate Change Initiative (47). The original resolution is 0.01° and we use conservative remapping to obtain a $1^\circ \times 1^\circ$ resolution. We use the daytime temperatures corresponding to the morning Terra equator crossing times at 10:30 local solar time. Small gaps in the data can occur close to the equator where the surface is not covered by the satellite swath on that day or globally when clouds are present since the IR radiometer will observe the cloud top that is usually much colder than the surface. We use data for 2001–2019 for figures including shortwave radiation and 2001–2018 for figures including surface temperature due to shorter data availability.

Monsoon Planet Model Configuration. The implemented atmospheric model GFDL-AM2 was created by GFDL to realistically simulate the dynamic, thermodynamic, and radiative components of the climate system (28). The primitive equations are solved on the sphere with Earth's radius (28, 48). The horizontal grid resolution is 2° latitude \times 2.5° longitude (28, 48), while the hybrid vertical grid consist of with 24 vertical levels ranging from 30 m above the surface to 3 hPa. The vertical resolution is decreasing toward higher altitudes. Advective and physics time steps are 10 min and 0.5 h (28), for atmospheric radiation 3 h time steps are chosen in order to include a diurnal cycle (48). In our setup, we choose preindustrial conditions (atmospheric CO_2 of 280 ppm, $1,361 \text{ W/m}^{-2}$) and exclude aerosols.

The atmosphere is coupled to a "slab-type" ocean model meaning that the ocean is represented by a horizontal grid of "slabs" of uniform depth (49). There is no interaction between the grid points, e.g. no ocean dynamics as currents, but the sea surface temperature at each grid point is resulting from the heat exchange across the air-sea and ocean-sea ice interfaces. The sea-ice model (50) is also run in "slab mode." The land is simulated with the land dynamics module LaD (51). Grassland with an albedo of 18.2 per cent is implemented as uniform vegetation type. The orography of these stripes is chosen to be without elevation. The implemented land dynamics module LaD (51) is based on the early model development of ref. 52, who simulates the continents as boxes with limited water storage. In the LaD module, additional physical processes are included as more complex representation of energy (e.g. sensible heat storage) and water storage (snowpack, root-zone water, and groundwater) (51). In the land model, a rudimentary runoff-routing scheme is implemented that transports water immediately to the closest ocean cell. Further information on the model configuration can be found in ref. 36.

Monsoon on the Monsoon Planet. The oscillation of the solar zenith angle between 23.5°S (December solstice) and 23.5°N (June solstice) forces changes in the surface temperature that is responding with a notable delay (*SI Appendix, Fig. S20*). This delay is particularly pronounced over oceanic regions due to distinct thermal properties. These characteristics of land and water also give rise to an asymmetric surface temperature distribution in the annual cycle. While areas strongly influenced by solar radiation during the Northern Hemisphere summer extend up to 60°N over land, comparable temperatures are only achieved up to 30°S over ocean during the Southern Hemisphere summer (*SI Appendix, Fig. S18*). Besides, the cooling impact of monsoon rainfall becomes evident north of the coast following the onset of the monsoon in June (*SI Appendix, Fig. S19*).

The surface temperature distribution shapes the formation of the associated high and low pressure systems. The low pressure area in tropical latitudes, the Inter-Tropical Convergence Zone, expands further poleward over land compared to the ocean on the Monsoon Planet—in line with real world observations. During the NH summer season, the warm rising air in the area of maximum surface temperature creates a substantial zone of low pressure over land, while a zone of relative high pressure over the tropical ocean south of the land forms. The surface pressure gradient translates in meridional surface winds from the high pressure region in the tropical ocean coastward. Arriving over the warmed land surface, the temperature of the moisture carrying air increases and rises, resulting in convective rainfall (*SI Appendix, Fig. S8*). It is important to note however, that the temperature gradient is strongest in May before the onset of the monsoon (*SI Appendix, Fig. S9*). During the winter months, these winds turn in the opposing direction toward the ocean—following the underlying surface pressure pattern (*SI Appendix, Figs. S21 and S22*). Given these changes in wind direction associated with different rainfall regimes, these dynamics classify as monsoon systems. The corresponding rainfall maximum over land (up to 12 mm/d) is referred to as summer monsoon reaching up to 25°N .

During the summer monsoon, a bimodality emerges in the rainfall distribution: While the meridional rainfall distribution is unimodal during the first months of the year, the originally single maximum begins to split in April, finally resulting in a clear bimodal rainfall distribution between June to September. One peak of the rainfall distribution is located over land, while the other rainfall maximum is located over the tropical ocean.

The average global annual rainfall is 807.6 mm. The global mean temperature on the Monsoon Planet is 16.8°C . From November to June, there is sea ice on the polar regions of the NH extending up to 60°N . From July to November there is sea ice on the SH extending also up to 60°S . The north of the land stripe (50 to 60°N) is seasonally covered with snow from October to April.

Robustness of Seasonal Hysteresis. We also analyze the hysteresis in simulations with varying solar insolation, carbon dioxide concentration, sulfate aerosol concentration as well as land albedo. The results show that the hysteresis is robust regarding changes in the baseline configuration that we use in this study. The memory effect varies depending on the underlying configuration and is particularly related to the global mean temperature: An increase in the global mean temperature strengthens the hysteresis and its memory effect. Higher temperatures increase evaporation over ocean, thus the water vapor availability increases. Besides, a warmer atmosphere is able to hold more moisture following the Clausius-Clapeyron relation. If the incoming radiation increases, also the temperature gradient between land and ocean strengthens the moisture transport from ocean toward land and reduces a barrier at the coast that can block moist surface winds (36). As a result, the availability, transport, and reservoir capacity of water vapor increases resulting in a stronger memory capacity of the system. Therefore, an increase of solar radiation increases the hysteresis (*SI Appendix, Fig. S10*). An increase of carbon dioxide and a decrease of aerosols have a similar effect (*SI Appendix, Figs. S11 and S12*). When increasing the surface albedo, the share of reflected radiation increases, while the absorbed radiation decreases. Thus, the surface warms comparatively less, reducing the monsoon-fueling effect of the low pressure system attracting moisture carrying winds from the ocean and finally reducing the hysteresis (*SI Appendix, Fig. S13*).

Data, Materials, and Software Availability. All model code used in this study is publicly available. The source code and example datasets for

the AM2 atmosphere model, the FMS coupler, and the LaD land model are available via the MOM5 Github repository (53). The code for the slab ocean model is also available on github (54). The codes required for producing the figures are available at <https://doi.org/10.5281/zenodo.15260911> (55), and the relevant simulation data can be downloaded from <https://doi.org/10.5281/zenodo.15260966> (56). The real-world climate data used in this study are publicly available from the references in the according subsection. All other data are included in the manuscript and/or *SI Appendix*.

ACKNOWLEDGMENTS. We would like to thank Jan Härter for an exciting discussion on tropical meteorology in which he pointed out the seasonal hysteresis in our simulations—a brief but insightful comment that inspired this study. This paper is supported within the scope of a Deutsche Gesellschaft für Internationale Zusammenarbeit project financed on behalf of

the Government of the Federal Republic of Germany and Federal Ministry for Economic Cooperation and Development (BMZ) under grant agreement No. 81290341. The Federal Ministry of Education and Research (BMBF) is funding the project PECan (The Political Economy of Climate Policy and Finance) within the framework of the Strategy "Research for Sustainability" (FONA) www.fona.de/en/ as part of its Social-Ecological Research funding priority, funding no. 01UU2205B. Responsibility for the content of this publication lies with the author. We also gratefully acknowledge the European Regional Development Fund, the German Federal Ministry of Education and Research and the Land Brandenburg for supporting this project by providing resources on the high-performance computer system at the Potsdam Institute for Climate Impact Research. The research was financially supported by the Heinrich-Boell Foundation. None of the funding partners have any influence on the study design, the data analysis or the interpretation of the results, or any other aspect.

1. D. C. Jiles, D. L. Atherton, Theory of ferromagnetic hysteresis. *J. Appl. Phys.* **55**, 2115–2120 (1984).
2. K. Røed, Hysteresis in unemployment. *J. Econ. Surv.* **11**, 389–418 (1997).
3. S. K. Kim *et al.*, Widespread irreversible changes in surface temperature and precipitation in response to CO₂ forcing. *Nat. Clim. Change* **12**, 834–840 (2022).
4. H. Oh *et al.*, Contrasting hysteresis behaviors of northern hemisphere land monsoon precipitation to CO₂ pathways. *Earths Future* **10**, e2021EF002623 (2022).
5. S. Paik, S. I. An, S. K. Min, A. D. King, J. Shin, Hysteric behavior of global to regional monsoon area under CO₂ ramp-up and ramp-down. *Earths Future* **11**, e2022EF003434 (2023).
6. A. Levermann, R. Winkelmann, A simple equation for the melt elevation feedback of ice sheets. *Cryosphere* **10**, 1799–1807 (2016).
7. M. I. Budyko, The effect of solar radiation variations on the climate of the earth. *Tellus* **21**, 611–619 (1969).
8. W. D. Sellers, A global climatic model based on the energy balance of the earth-atmosphere system. *J. Appl. Meteorol.* **1962-1982**, 392–400 (1969).
9. V. Lucarini, K. Fraedrich, F. Lunkeit, Thermodynamic analysis of snowball earth hysteresis experiment: Efficiency, entropy production and irreversibility. *Q. J. R. Meteorol. Soc. J. Atmos. Sci. Appl. Meteorol. Phys. Oceanogr.* **136**, 2–11 (2010).
10. J. Garbe, T. Albrecht, A. Levermann, J. F. Donges, R. Winkelmann, The hysteresis of the Antarctic ice sheet. *Nature* **585**, 538–544 (2020).
11. A. Robinson, R. Calov, A. Ganopolski, Multistability and critical thresholds of the Greenland ice sheet. *Nat. Clim. Change* **2**, 429–432 (2012).
12. H. Stommel, A. Arons, On the abyssal circulation of the world ocean—I. Stationary planetary flow patterns on a sphere. *Deep Sea Res.* **6**, 140–154 (1959).
13. S. Rahmstorf, On the freshwater forcing and transport of the Atlantic thermohaline circulation. *Clim. Dyn.* **12**, 799–811 (1996).
14. S. I. An *et al.*, Global cooling hiatus driven by an AMOC overshoot in a carbon dioxide removal scenario. *Earths Future* **9**, e2021EF002165 (2021).
15. C. Liu *et al.*, Hysteresis of the El Niño-southern oscillation to CO₂ forcing. *Sci. Adv.* **9**, eadh8442 (2023).
16. E. Maier-Reimer, K. Hasselmann, Transport and storage of CO₂ in the ocean—an inorganic ocean-circulation carbon cycle model. *Clim. Dyn.* **2**, 63–90 (1987).
17. K. B. Tokarska, K. Zickfeld, The effectiveness of net negative carbon dioxide emissions in reversing anthropogenic climate change. *Environ. Res. Lett.* **10**, 094013 (2015).
18. A. Jeltsch-Thömmes, T. F. Stocker, F. Joos, Hysteresis of the earth system under positive and negative CO₂ emissions. *Environ. Res. Lett.* **15**, 124026 (2020).
19. A. Staal *et al.*, Hysteresis of tropical forests in the 21st century. *Nat. Commun.* **11**, 4978 (2020).
20. J. S. Kug *et al.*, Hysteresis of the intertropical convergence zone to CO₂ forcing. *Nat. Clim. Change* **12**, 47–53 (2022).
21. J. Hwang *et al.*, Asymmetric hysteresis response of mid-latitude storm tracks to CO₂ removal. *Nat. Clim. Change* **14**, 1–8 (2024).
22. P. Wu, R. Wood, J. Ridley, J. Lowe, Temporary acceleration of the hydrological cycle in response to a CO₂ rampdown. *Geophys. Res. Lett.* **37**, 043730 (2010).
23. R. Chadwick, P. Wu, P. Good, T. Andrews, Asymmetries in tropical rainfall and circulation patterns in idealised CO₂ removal experiments. *Clim. Dyn.* **40**, 295–316 (2013).
24. K. Zickfeld, B. Knopf, V. Petoukhov, H. Schellnhuber, Is the Indian summer monsoon stable against global change? *Geophys. Res. Lett.* **32**, 022771 (2005).
25. C. S. Ramage, *Monsoon Meteorology* (Academic Press, 1971).
26. D. L. Hartmann, *Global Physical Climatology* (Elsevier, ed. 2, 2016), vol. 103.
27. K. E. Trenberth, D. P. Stepaniak, J. M. Caron, The global monsoon as seen through the divergent atmospheric circulation. *J. Clim.* **13**, 3969–3993 (2000).
28. GFDL-Global-Atmospheric-Model-Development-Team *et al.*, The new GFDL global atmosphere and land model AM2-LM2. *J. Clim.* **17**, 4641–4673 (2004).
29. P. Masson-Delmotte *et al.*, *Climate Change 2021: The Physical Science Basis. Contribution of Working Group I to the Sixth Assessment Report of the Intergovernmental Panel on Climate Change* (Cambridge University Press, 2021).
30. A. Kitoh *et al.*, Monsoons in a changing world: A regional perspective in a global context. *J. Geophys. Res. Atmos.* **118**, 3053–3065 (2013).
31. B. Wang, Q. Ding, Global monsoon: Dominant mode of annual variation in the tropics. *Dyn. Atmos. Oceans* **44**, 165–183 (2008).
32. K. A. Emanuel, J. David Neelin, C. S. Bretherton, On large-scale circulations in convecting atmospheres. *Q. J. R. Meteorol. Soc.* **120**, 1111–1143 (1994).
33. N. C. Privé, R. A. Plumb, Monsoon dynamics with interactive forcing. Part I: Axisymmetric studies. *J. Atmos. Sci.* **64**, 1417–1430 (2007).
34. W. Zhou, S. P. Xie, A hierarchy of idealized monsoons in an intermediate GCM. *J. Clim.* **31**, 9021–9036 (2018).
35. R. Geen, S. Bordoni, D. S. Battisti, K. Hui, Monsoons, ITCZs, and the concept of the global monsoon. *Rev. Geophys.* **58**, e2020RG000700 (2020).
36. A. Katzenberger, S. Petri, G. Feulner, A. Levermann, Monsoon planet: Bimodal rainfall distribution due to barrier structure in pressure fields. *J. Clim.* **37**, 1295–1315 (2024).
37. G. C. Simpson, The south-west monsoon. *Q. J. R. Meteorol. Soc.* **47**, 151–171 (1921).
38. L. F. Richardson, *Weather Prediction by Numerical Process* (University Press, 1922).
39. J. R. Holton, *An Introduction to Dynamic Meteorology* (American Association of Physics Teachers, 1973), vol. 41.
40. A. Levermann, J. Schewe, V. Petoukhov, H. Held, Basic mechanism for abrupt monsoon transitions. *Proc. Natl. Acad. Sci. U.S.A.* **106**, 20572–20577 (2009).
41. G. Dagan, N. Yeheskel, A. I. Williams, Radiative forcing from aerosol-cloud interactions enhanced by large-scale circulation adjustments. *Nat. Geosci.* **16**, 1–7 (2023).
42. R. Mallesh, J. Srinivasan, How is the relationship between rainfall and water vapor in the Indian monsoon influenced by changes in lapse rate during global warming? *Environ. Res. Commun.* **6**, ad2c64 (2024).
43. M. Colin, S. Sherwood, O. Geoffroy, S. Bony, D. Fuchs, Identifying the sources of convective memory in cloud-resolving simulations. *J. Atmos. Sci.* **76**, 947–962 (2019).
44. A. Levermann *et al.*, Potential climatic transitions with profound impact on Europe - Review of the current state of six 'tipping elements of the climate system.' *Clim. Change* **110**, 845–878 (2012).
45. N. G. Loeb *et al.*, Clouds and the earth's radiant energy system (CERES) energy balanced and filled (EBAF) top-of-atmosphere (TOA) edition-4.0 data product. *J. Clim.* **31**, 895–918 (2018).
46. M. Ziese *et al.*, GPCC Full Data Daily Version 2020 at 1.0°: Daily Land-Surface Precipitation from Rain-Gauges built on GTS-based and Historic Data. http://dx.doi.org/10.5676/DWD_GPCC/FD_D_V2020_100. Accessed 22 April 2025.
47. D. Ghent, K. Veal, M. Perry, ESA Land Surface Temperature Climate Change Initiative (LST_cci): Monthly land surface temperature from MODIS (Moderate resolution Infra-red Spectroradiometer) on Terra, level 3 collated (L3C) global product (2000-2018), version 3.00 (2022). <https://dx.doi.org/10.5285/32d7bc64c7b740e9ad7a43589ab91592>. Accessed 22 April 2025.
48. T. L. Delworth *et al.*, GFDL's CM2 global coupled climate models. Part I: Formulation and simulation characteristics. *J. Clim.* **19**, 643–674 (2006).
49. R. J. Stouffer *et al.*, GFDL's CM2 global coupled climate models. Part IV: Idealized climate response. *J. Clim.* **19**, 723–740 (2006).
50. M. Winton, A reformulated three-layer sea ice model. *J. Atmos. Oceanic Technol.* **17**, 525–531 (2000).
51. P. Milly, A. Shmakin, Global modeling of land water and energy balances. Part I: The land dynamics (LaD) model. *J. Hydrometeorol.* **3**, 283–299 (2002).
52. S. Manabe, Climate and the ocean circulation: I. The atmospheric circulation and the hydrology of the earth's surface. *Mon. Weather Rev.* **97**, 739–774 (1969).
53. S. Griffies *et al.*, MOM5 Modular Ocean Model. Web Site. <https://mom-ocean.github.io/>. Accessed 18 April 2025.
54. GFDL Team, GFDL FMS Slab Ocean Model. Repository. <https://www.gfdl.noaa.gov/fms-slab-ocean-model-technical-documentation/>. Accessed 18 April 2025.
55. A. Katzenberger, AnjaKatzenberger/Monsoon_Hysteresis_reveals_Atmospheric_Memory: Codes for Publication 'Monsoon Hysteresis reveals Atmospheric Memory' (v1.0). Zenodo. <https://doi.org/10.5281/zenodo.15260911>. Deposited 22 April 2025.
56. A. Katzenberger, A. Levermann, Data for Publication 'Monsoon Hysteresis reveals Atmospheric Memory' (v1.0) [Data set]. Zenodo. <https://doi.org/10.5281/zenodo.15260966>. Deposited 22 April 2025.

Supplementary Information: Monsoon Hysteresis reveals Atmospheric Memory

Anja Katzenberger,^{1,2} Anders Levermann,^{1,2,3*}

¹Potsdam Institute for Climate Impact Research, Potsdam, Germany

²Institute for Physics and Astronomy, Potsdam University, Potsdam, Germany

³LDEO, Columbia University, New York, USA

*To whom correspondence should be addressed; E-mail: anders.levermann@pik-potsdam.de

Additional information supporting the manuscript "Monsoon Hysteresis reveals Atmospheric Memory" by Katzenberger, A. and Levermann, A.

Supplementary Figures

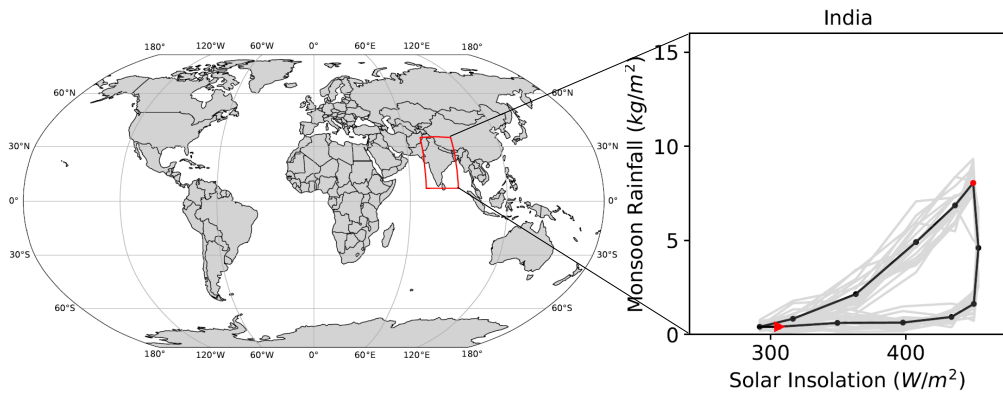


Figure S1: **Hysteresis of observed Indian Monsoon over larger underlying region.** As in Fig. 1 but for a larger region over India including adjacent ocean regions. The hysteresis also sustains when the region underlying the analysis is varied or enlarged.

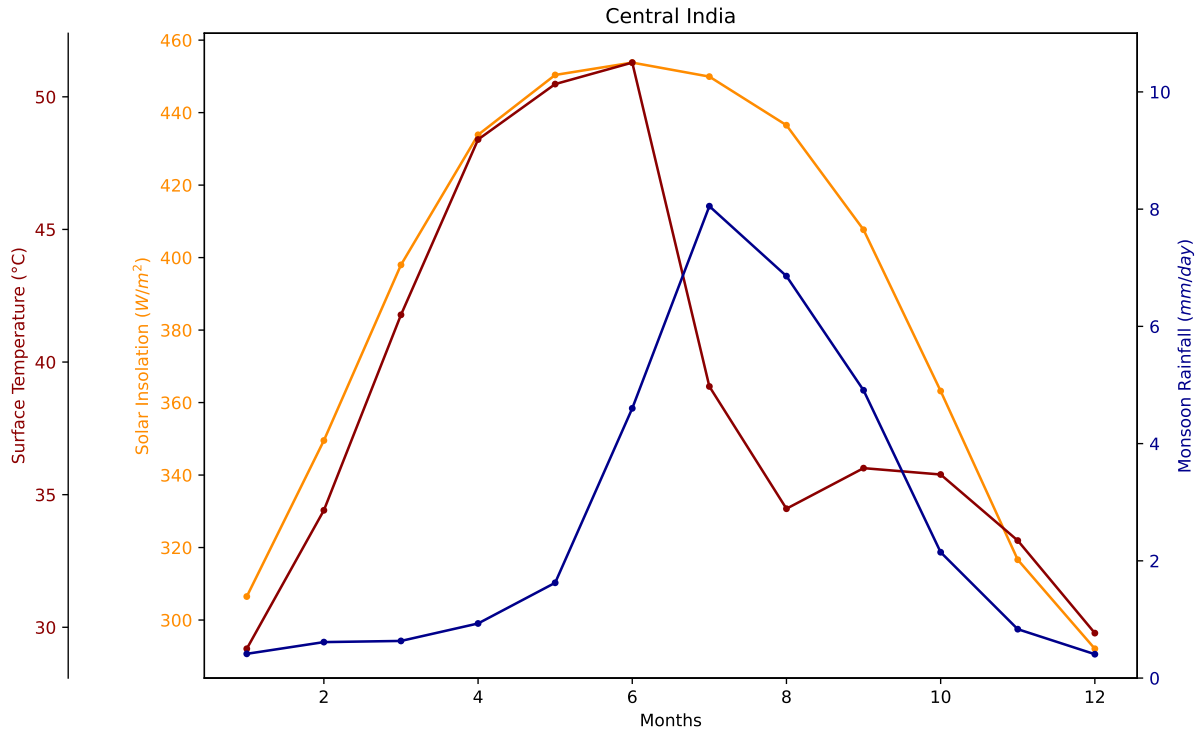


Figure S2: **General characteristics of the Indian Monsoon throughout the year.** Climate Data Source: TERRA MODIS for surface temperature, GPCP for rainfall, CERES for radiation, see SI. Monthly averages from 18 years are shown. Underlying region over Central India is 17-26 °N and 76-82°E.

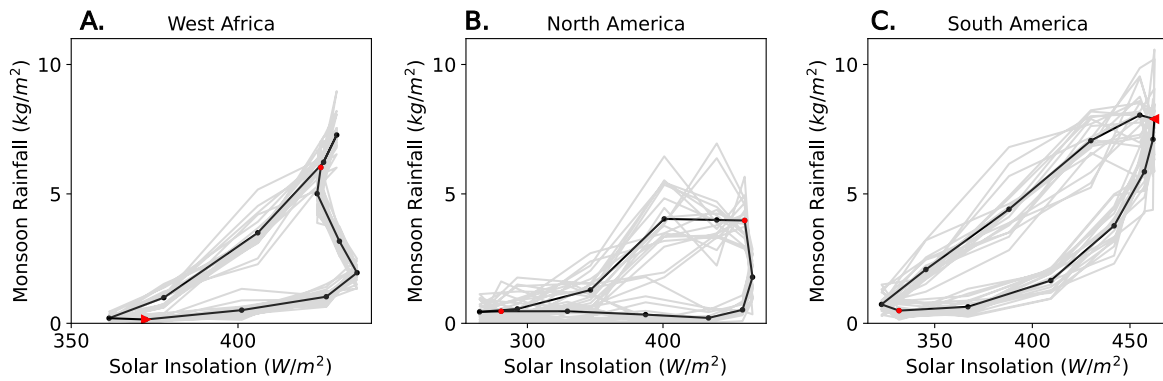


Figure S3: **Hysteresis in further observed monsoon systems.** As in Fig. 1 but for the West African, North American and South American monsoon. Underlying regions are shown in Fig. S4.

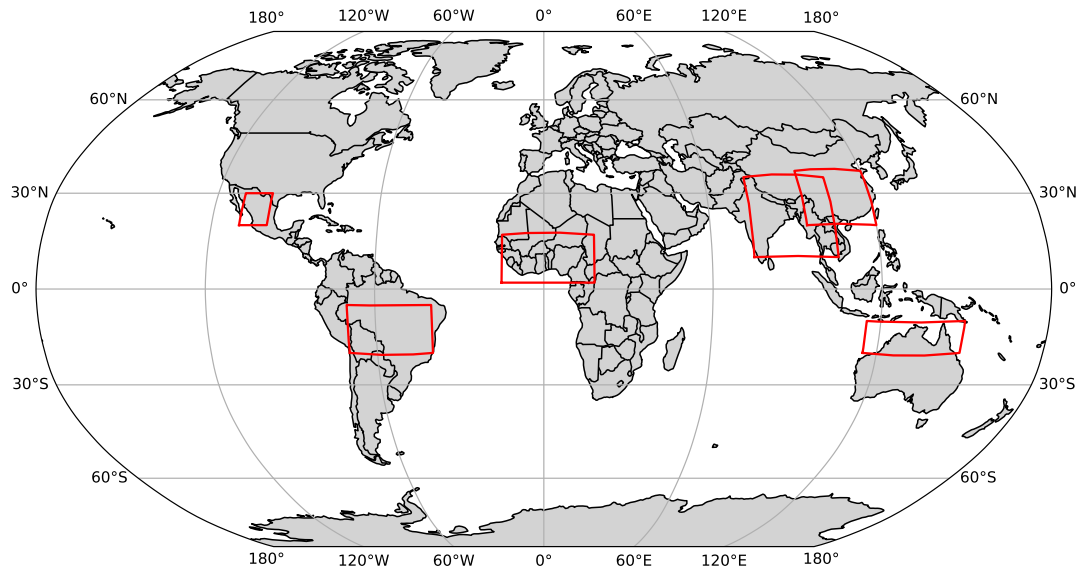


Figure S4: Areas of regional monsoon systems. Regional monsoon areas as used for Fig. 1 and S3 including the North American Monsoon (20-30°N, 110-100°W), South American Monsoon (5-20°S, 40-70°W), West African Monsoon (2-17°N, 15°W -18°E), Monsoon over the Bay of Bengal (10-35°N, 75-105°E), the East Asian Monsoon (20-37°N, 95-120°E) and the Australian Monsoon (10-20°S, 115-150°E). The results are robust regarding variations of the underlying region.

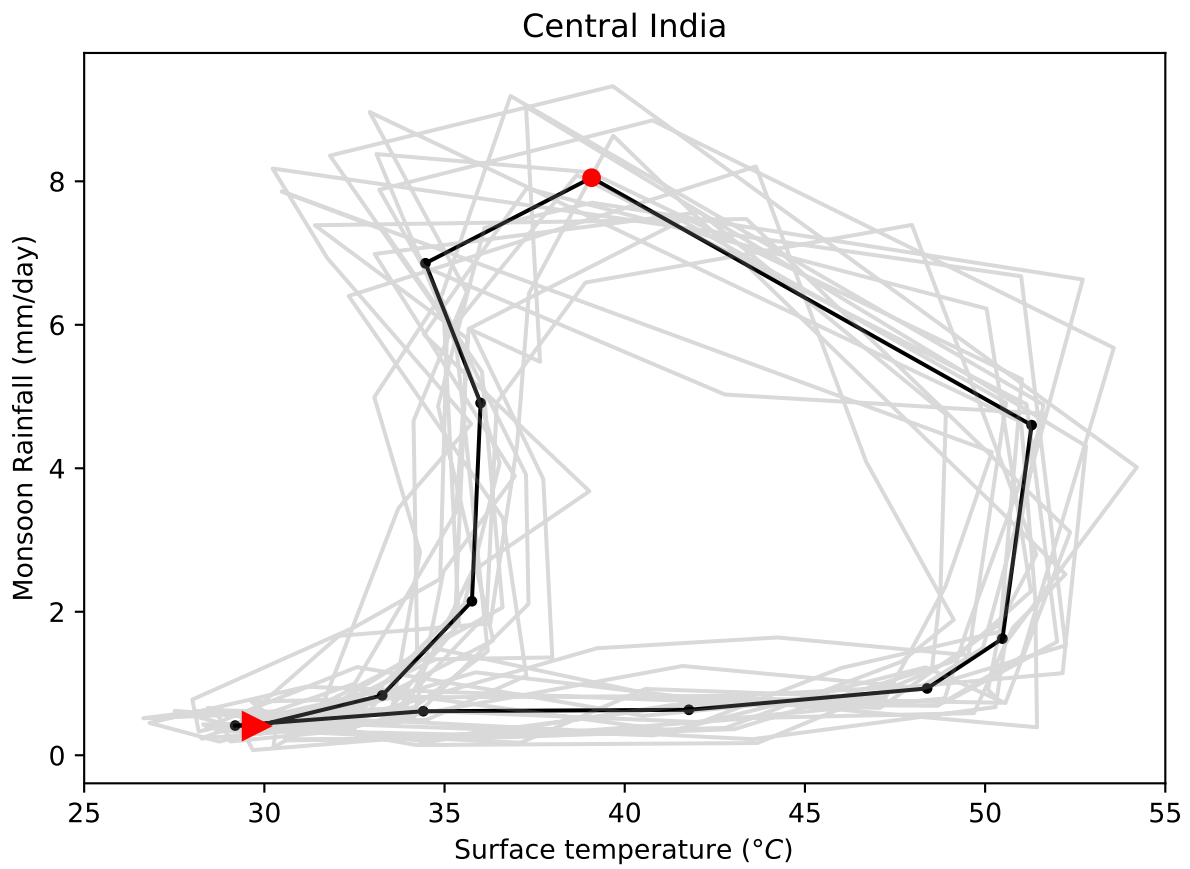


Figure S5: **Observed seasonal monsoon hysteresis in India depending on surface temperature.** As in Fig. 1 but in dependence of surface temperature. Climate Data Source: TERRA MODIS for surface temperature, GPCP for rainfall, see SI. Monthly data for 2001-2018 is shown.

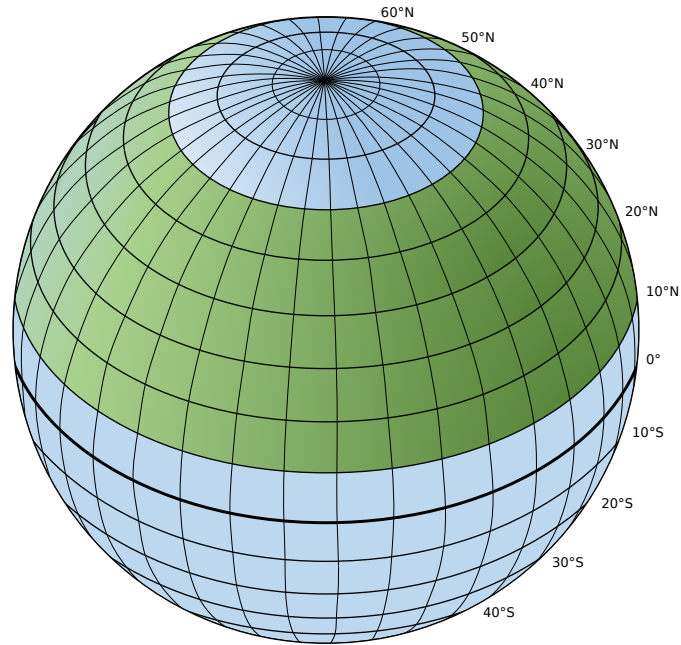


Figure S6: **Monsoon Planet - Model Setup.** Aquaplanet with circumglobal landstripe ranging from 10 to 60°N of uniform altitude, vegetation type (grassland) and albedo (18.2 per cent).

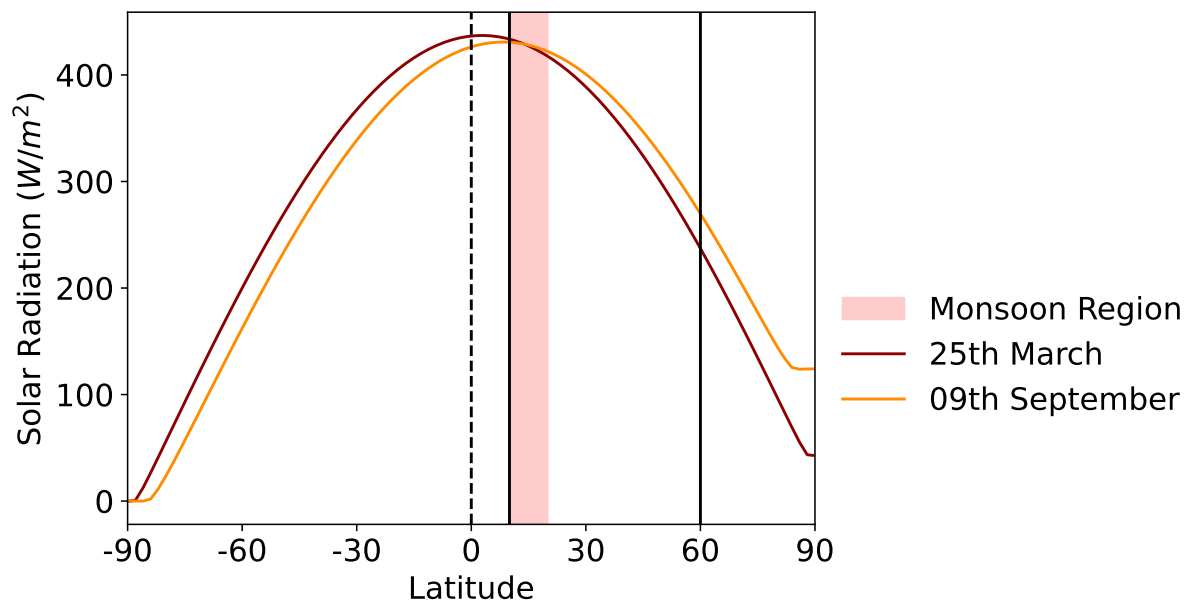


Figure S7: **Meridional profile of solar forcing for two dates.** The incoming shortwave solar radiation for two dates is shown. The dates are chosen such that the average radiation over the red marked monsoon region is the same. The vertical dashed line marks the equator, the continuous line indicates the location of land.

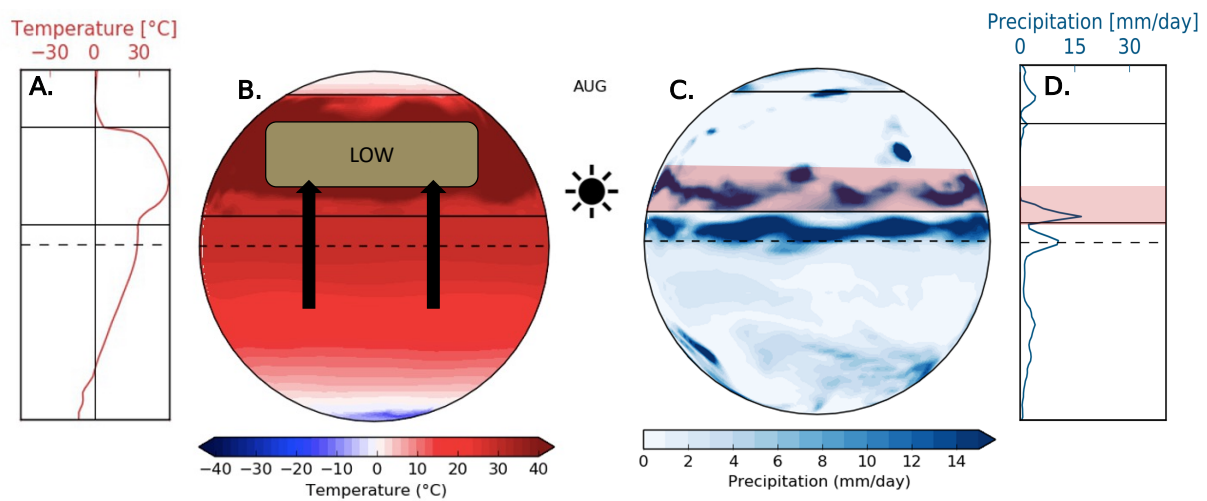


Figure S8: **Meridional monsoon circulation on the Monsoon Planet.** The continuous horizontal line marks the location of land, the horizontal dashed line indicates the equator. August as exemplary monsoon month with the zenith angle over the Northern Hemisphere (marked by sun symbol) is shown. The summer solar insolation warms the land (panel A) and creates a low pressure system over land attracting moisture carrying winds from the ocean (panel B). These winds rise when they reach land and result in convective rainfall over land (panel C). Given its seasonality, this classifies as monsoon rainfall (shaded in red). The meridional rainfall distributions (panel D) is bimodal during the monsoon season.

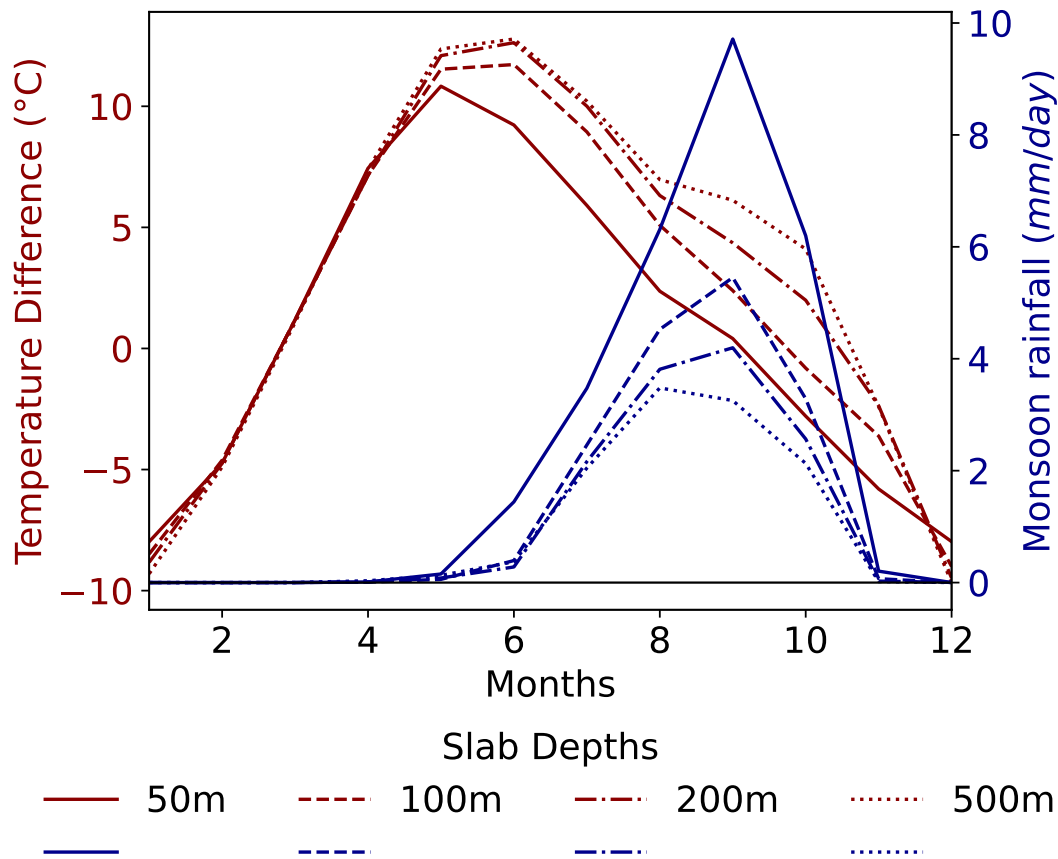


Figure S9: **Surface temperature gradient and Monsoon rainfall throughout the year for different slab depths.** The temperature difference is calculated as land (10-20°N) minus adjacent ocean (0-10°N) temperature. The 20-years monthly averages are shown.

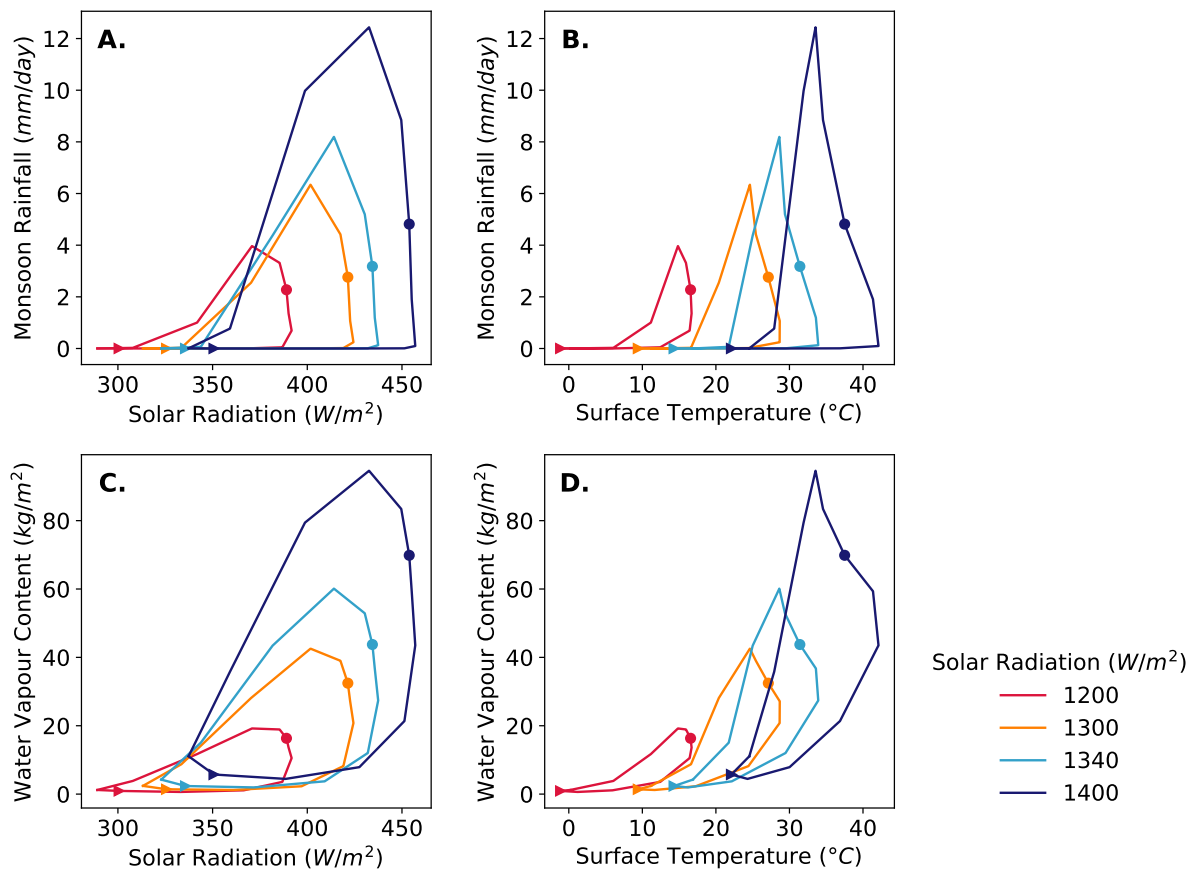


Figure S10: **Robustness of the hysteresis dynamics regarding varying solar radiation.** As in Fig. 2A but with varying solar radiation. The 20-years monthly averages are shown for the region 10-20 $^{\circ}N$.

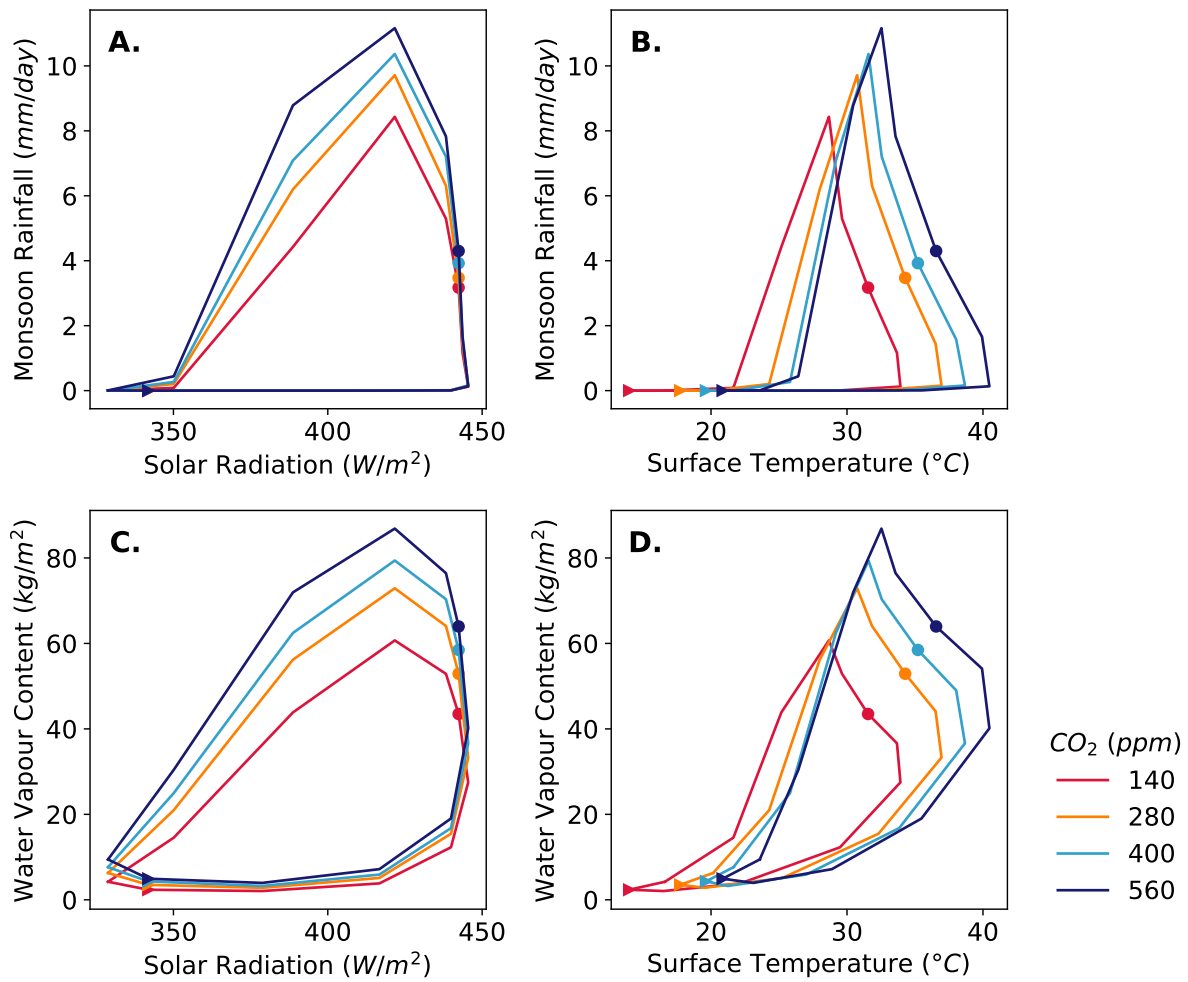


Figure S11: **Robustness of the hysteresis dynamics regarding varying atmospheric CO₂ concentration.** As in Fig. 2A but with varying CO₂ concentrations. The 20-years monthly averages are shown for the region 10-20°N.

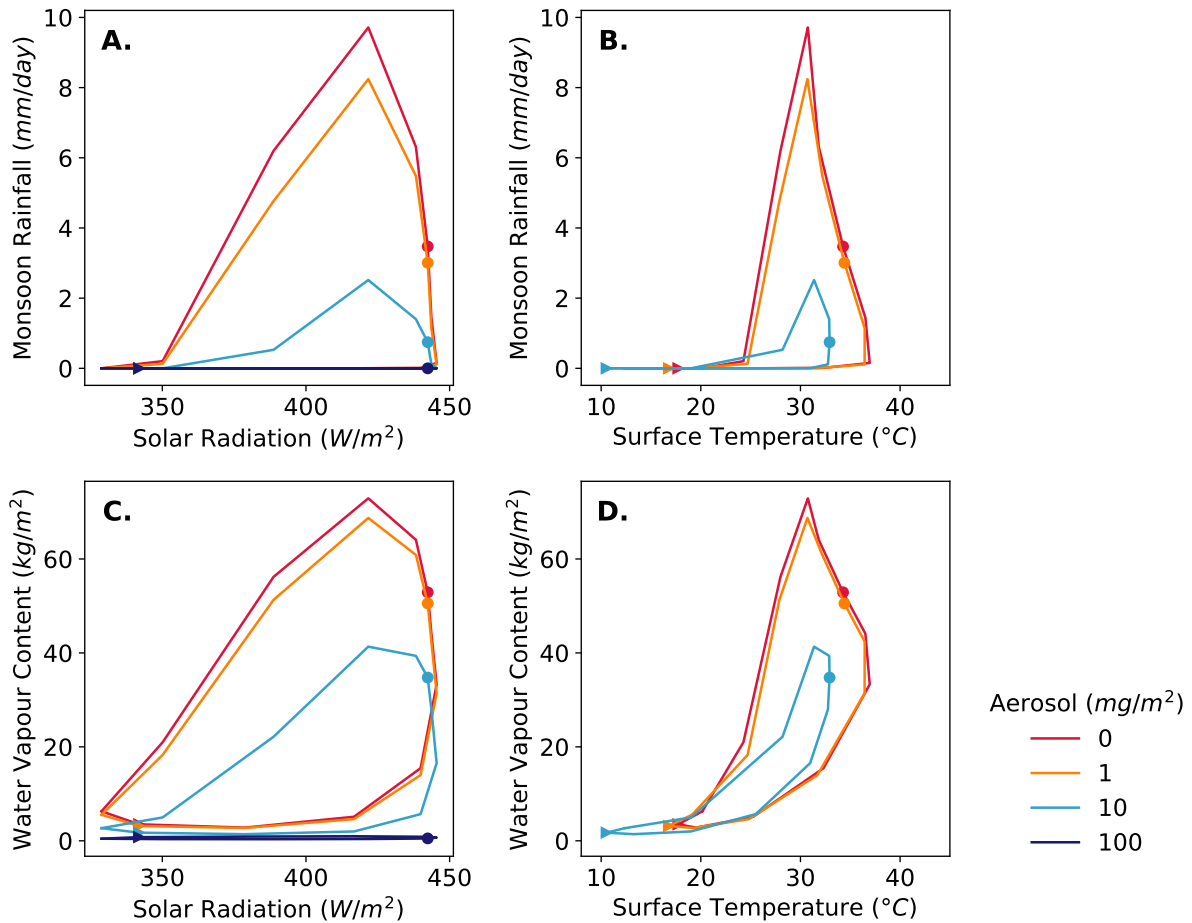


Figure S12: **Robustness of the hysteresis dynamics regarding varying atmospheric sulfate aerosol concentration.** As in Fig. 2A but with varying aerosol concentrations. The surface temperature for the simulation with 100 mg/m^3 ranges from -14.2° to 3.4° and is therefore not displayed. The 20-years monthly averages are shown for the region 10-20 $^{\circ}$ N.

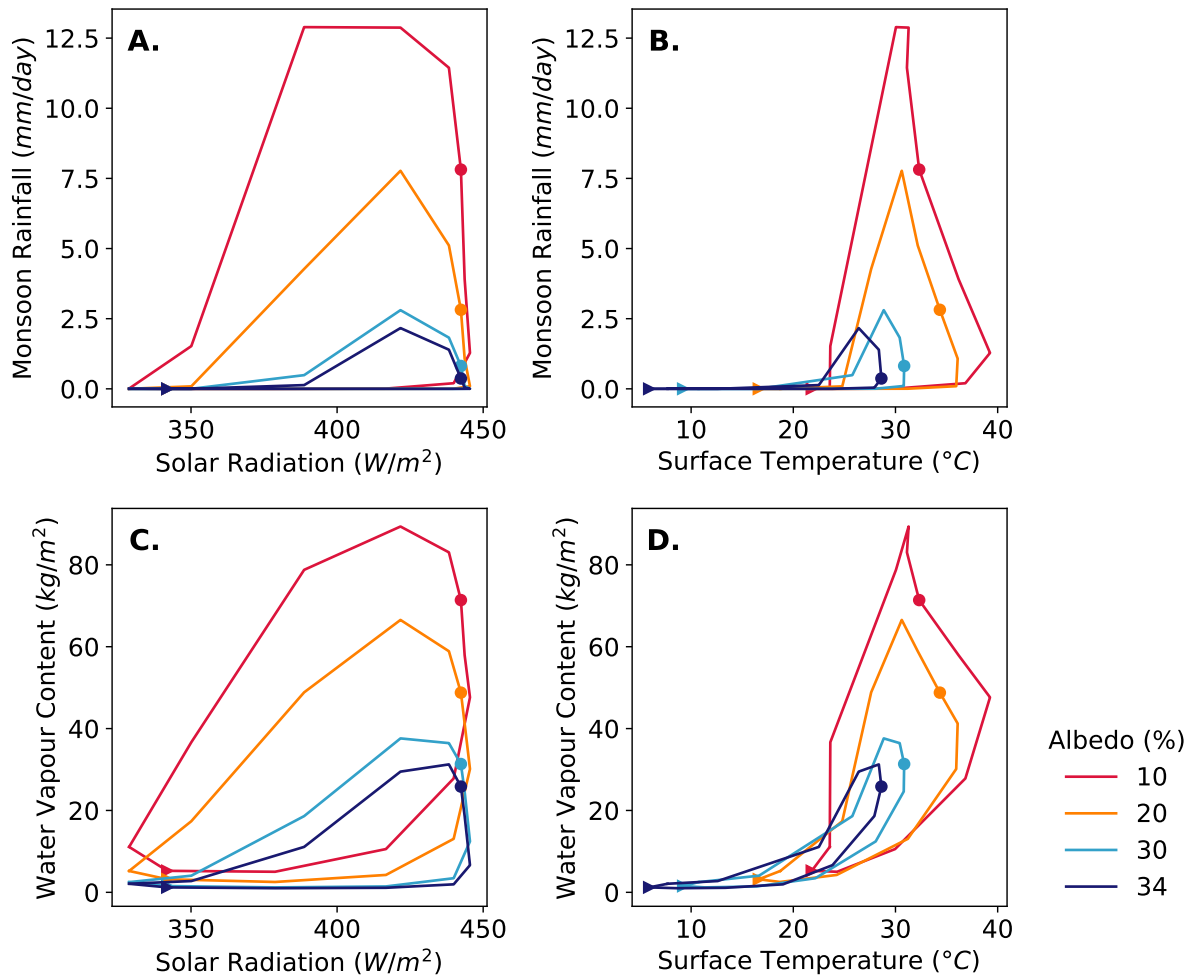


Figure S13: **Robustness of the hysteresis dynamics regarding varying land surface albedo.** As in Fig. 2A but with varying albedo. The 20-years monthly averages are shown for the region 10-20 $^{\circ}$ N.

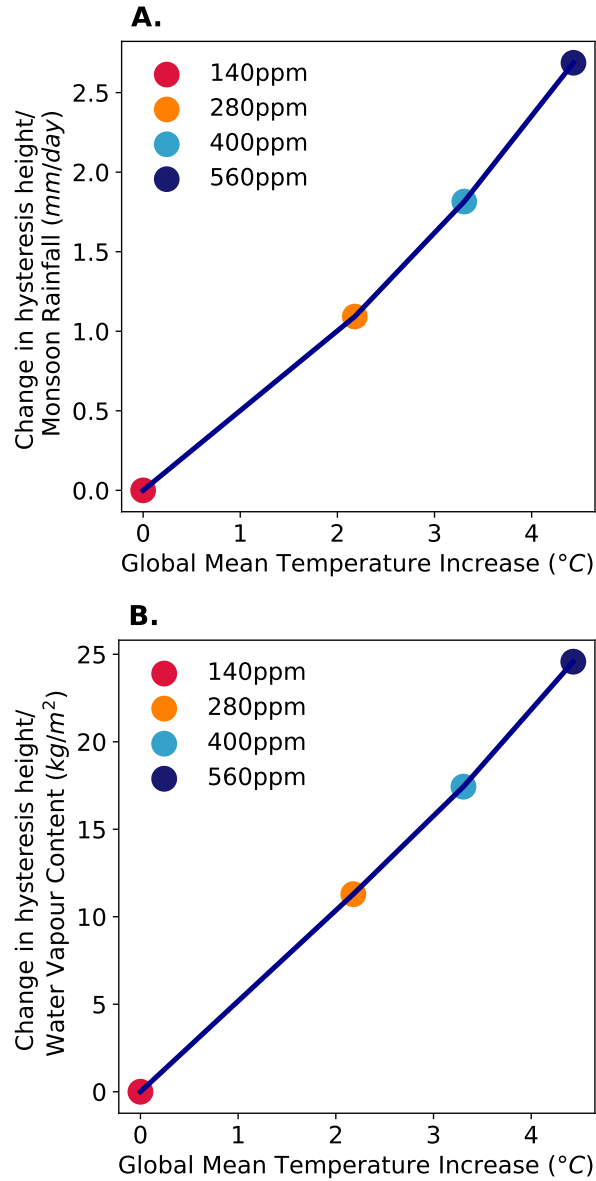


Figure S14: **Hysteresis under global warming induced by increasing levels of carbon dioxide.** The height of the hysteresis regarding rainfall changes (panel A) and water vapour content changes (panel B) averaged over the monsoon region (10-20°N) and over the monsoon season on the idealized setup (July to October) depending on the global mean temperature increase is shown in blue.

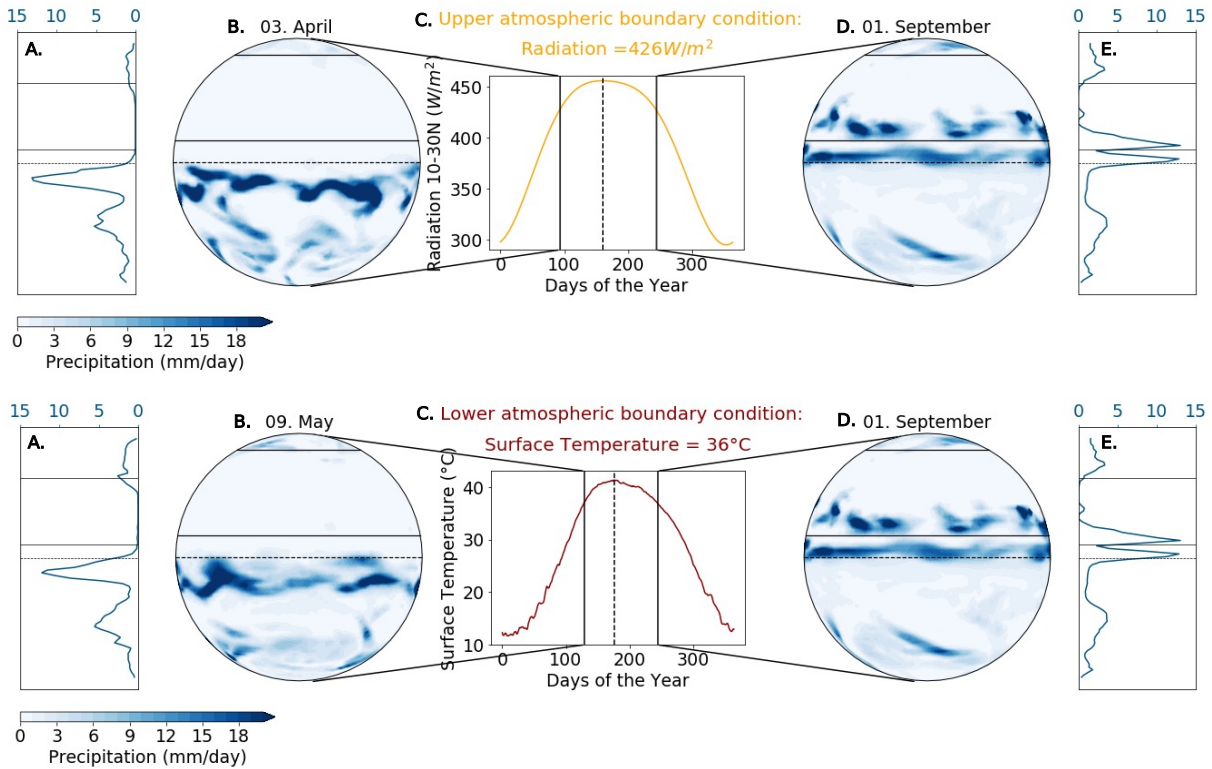


Figure S15: **Precipitation distribution on the Monsoon Planet for two dates with equal boundary conditions (solar radiation, surface temperature) but differing rainfall in the monsoon region.** Panel A-E: Incoming solar radiation at the top of the atmosphere as upper atmospheric boundary condition. Panel C: The solar radiation throughout the year is shown in orange. The dashed line marks the maximum of the distribution on 9th June and the vertical black lines indicate the two days with a solar radiation of 426 W/m^2 . Panel B, D show the associated global rainfall distribution for these two dates. Horizontal continuous lines mark the location of land, the horizontal dashed line the equator. Panel A, E provide the meridional average for both states with continuous lines for land location and dashed lines for the equator. Panel E-J: Same as panels A-D but for lower boundary conditions. The surface temperature (red) peaks on 25th June (dashed vertical line) and the continuous vertical lines mark the two days with a surface temperature of 36°C .

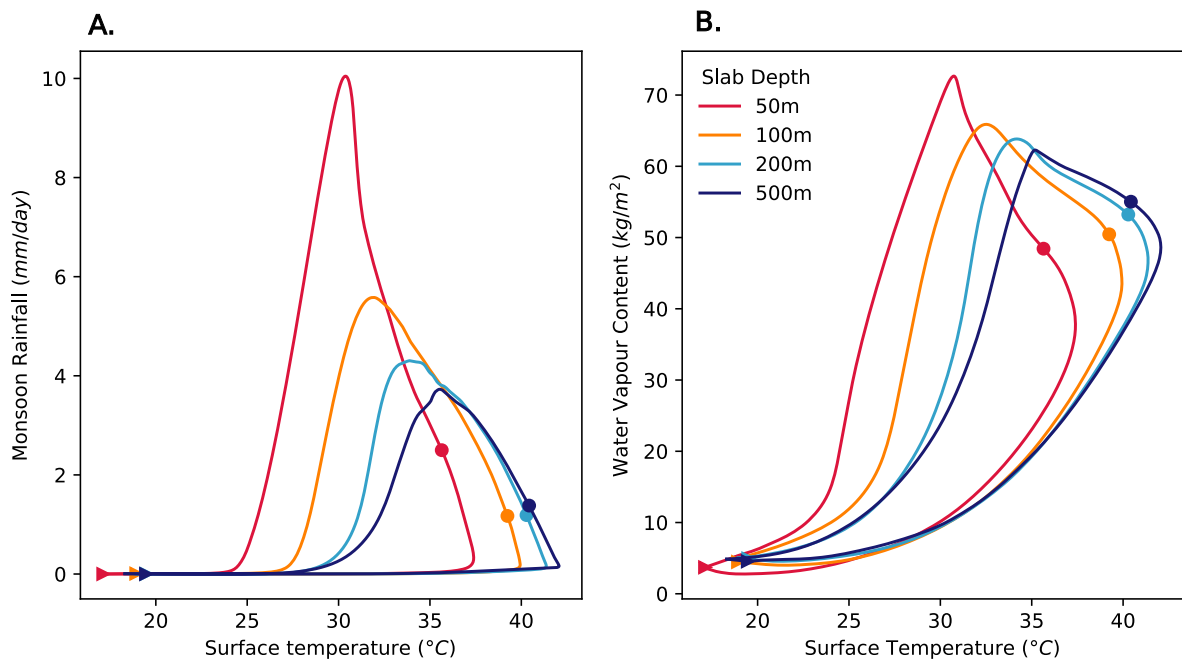


Figure S16: **Monsoon rainfall depending on the lower boundary conditions (surface temperature).** As in Fig. 2A/B, but for surface temperature as lower boundary conditions.

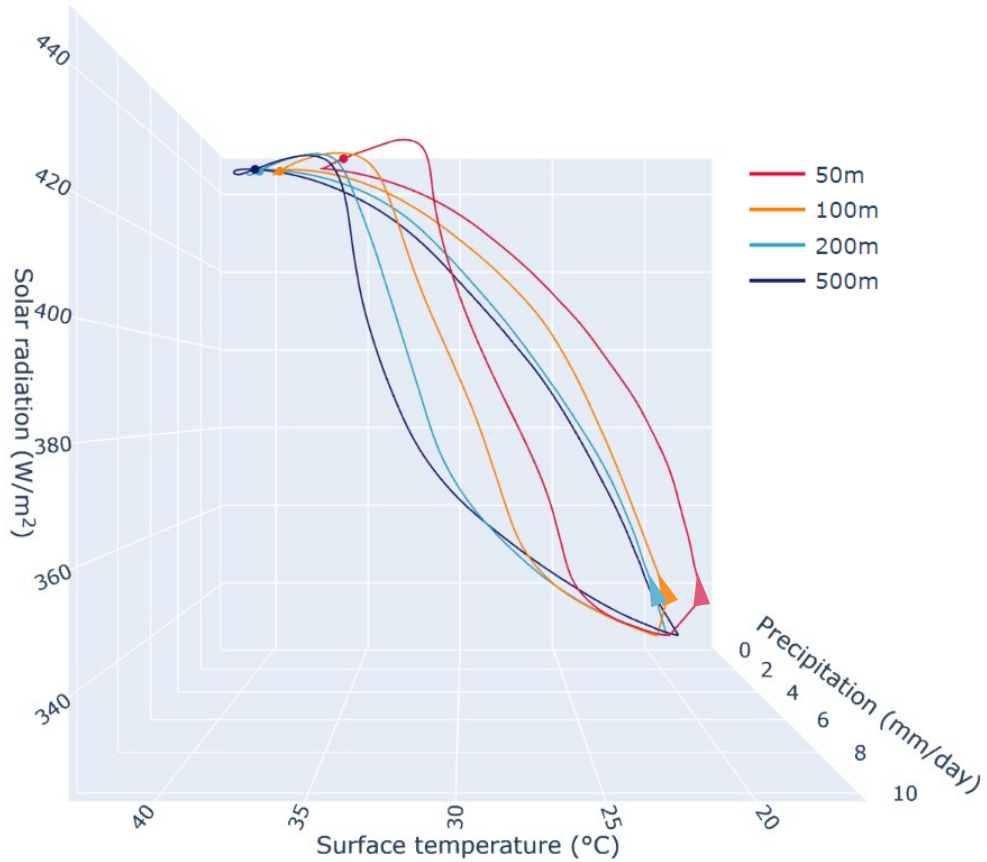


Figure S17: **Monsoon rainfall depending on its upper (solar radiation) and lower (surface temperature) boundary conditions.** The 10-years average of daily data smoothed by singular spectrum analysis is shown. Colors and markers as in Fig. 2A. Results for the monsoon region (10-20°N) are presented. An interactive 3-dimensional version of this figure is available, see data availability statement.

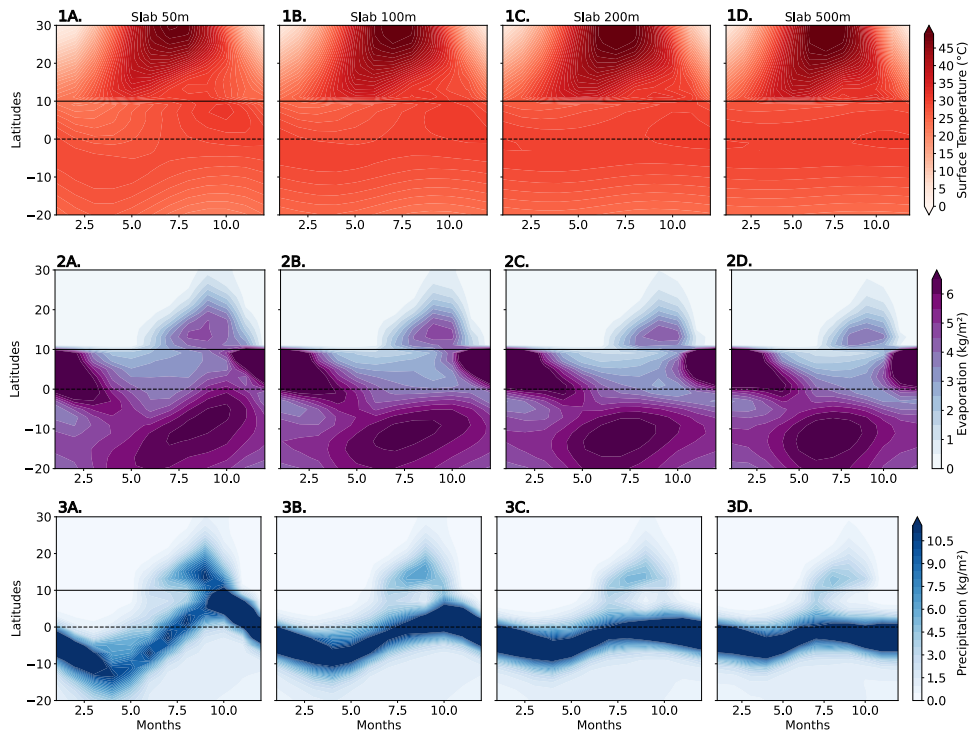


Figure S18: **General characteristics of the Monsoon Planet with varying slab ocean depths.** Surface temperature (1A-D), evaporation (2A-D), and precipitation (3A-D) for 20°S to 30°N with slab ocean depths of 50m, 100m, 200m, 500m. The continuous horizontal line marks the equator, the dashed horizontal line the location of land. The 20-years monthly averages are shown.

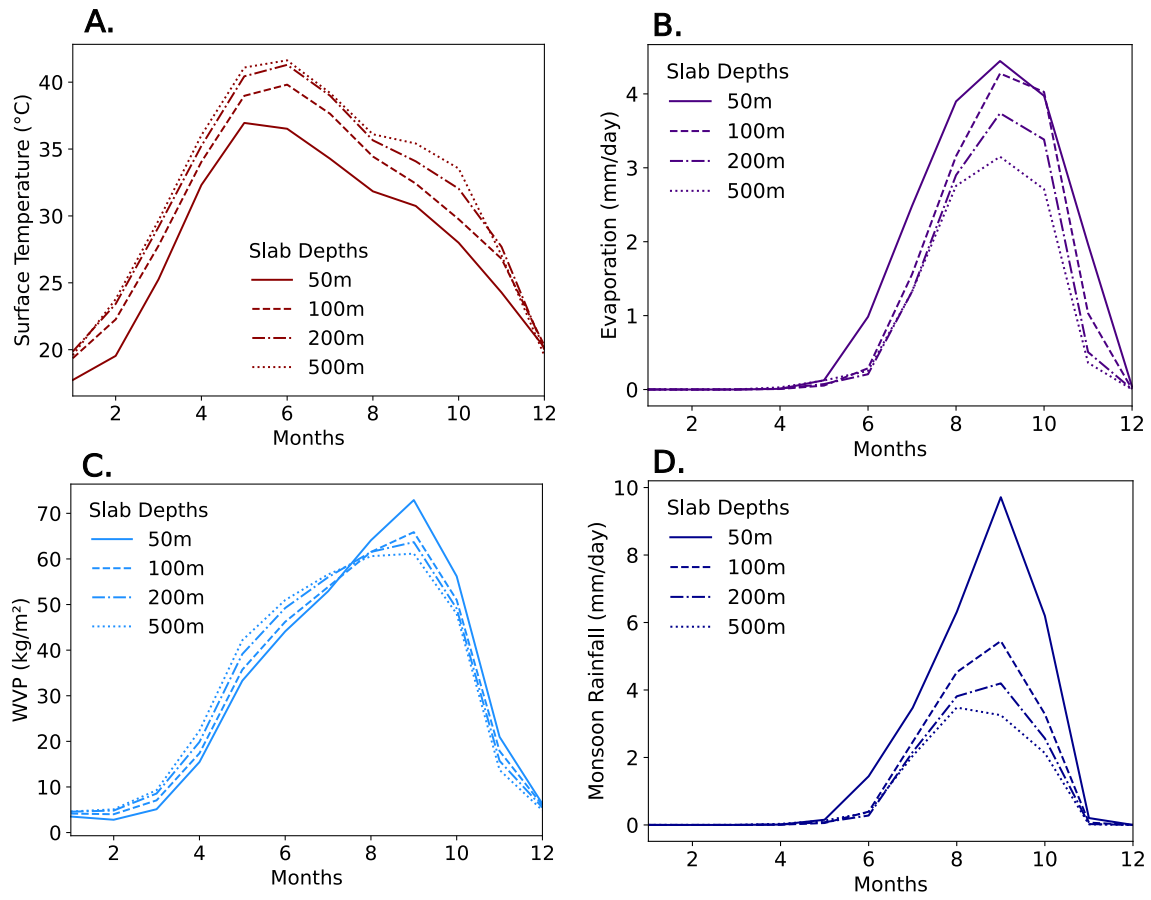


Figure S19: **General Characteristics for the monsoon region (10-20°N) on the Monsoon Planet throughout the year with varying slab ocean depths.** Surface temperature (panel A), evaporation (panel B), column integrated water vapor (WVP; panel C), and monsoon rainfall (panel D) for the Monsoon Planet with slab depths of 50m, 100m, 200m, 500m. The 20-years monthly averages are shown.

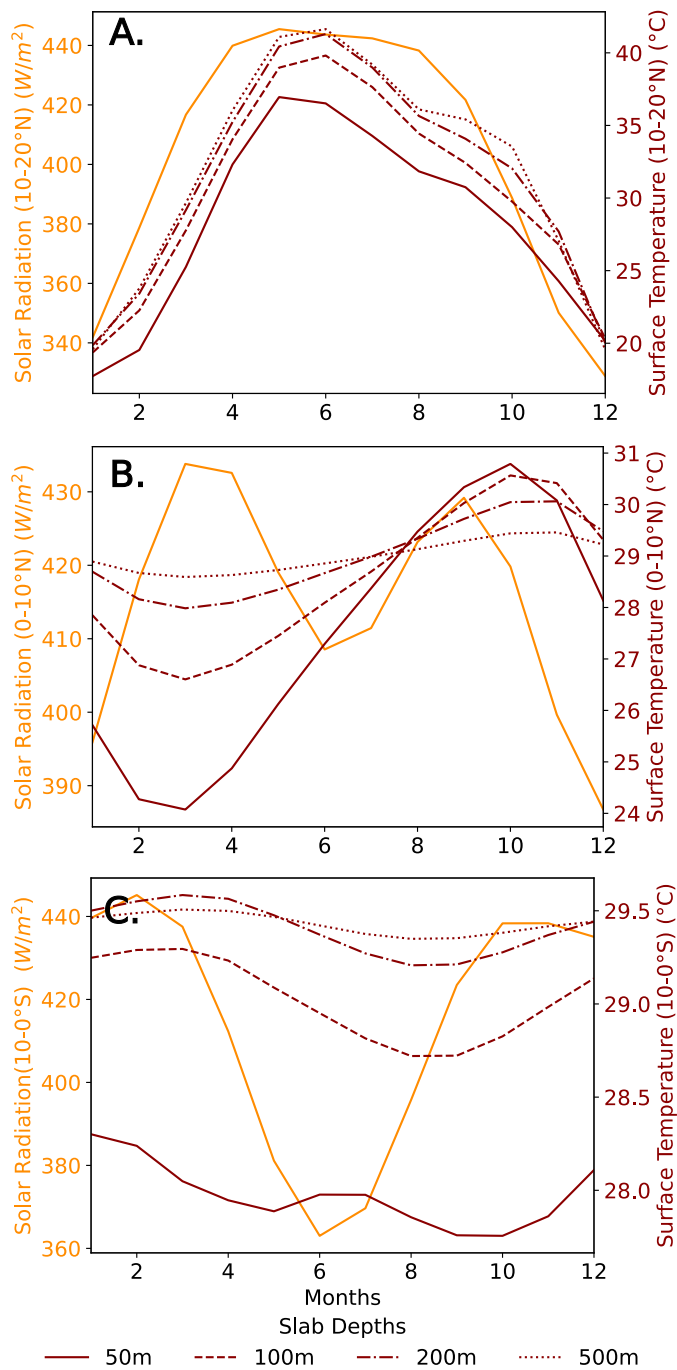


Figure S20: **Solar radiation and consequent warming of the monsoon region (panel A: 10-20°N), the northern (panel B: 0-10°N) and the southern equatorial ocean (panel C: 10°S) for different slab depths throughout the year.** Solar radiation refers to the incoming shortwave radiation at the top of the atmosphere. The 20-years monthly averages are shown.

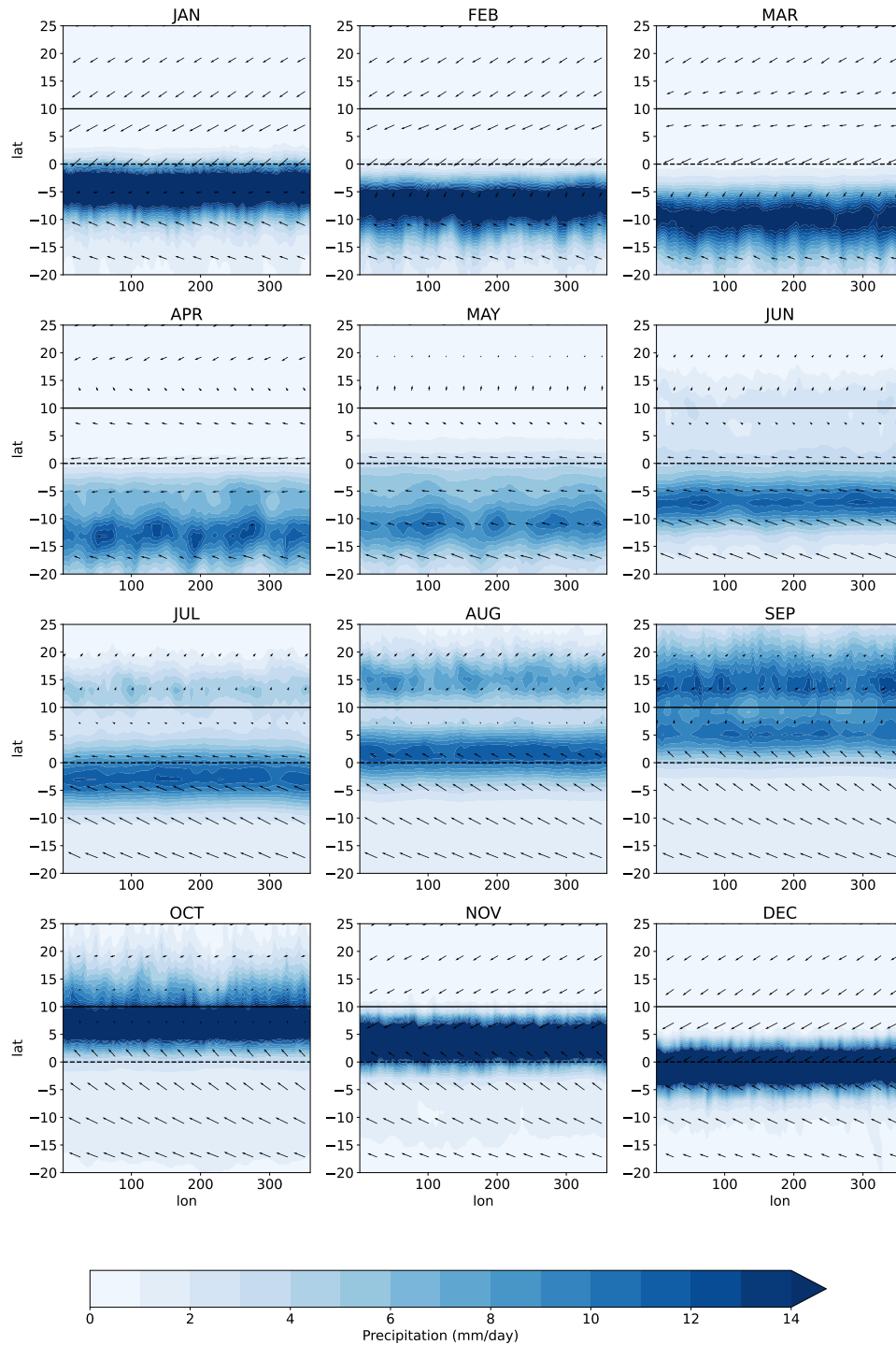


Figure S21: **Precipitation and surface wind direction for the Monsoon Planet throughout the year with slab ocean depth of 50m.** The continuous horizontal line marks the equator, the dashed horizontal line the location of land. The 20-years monthly averages are shown.

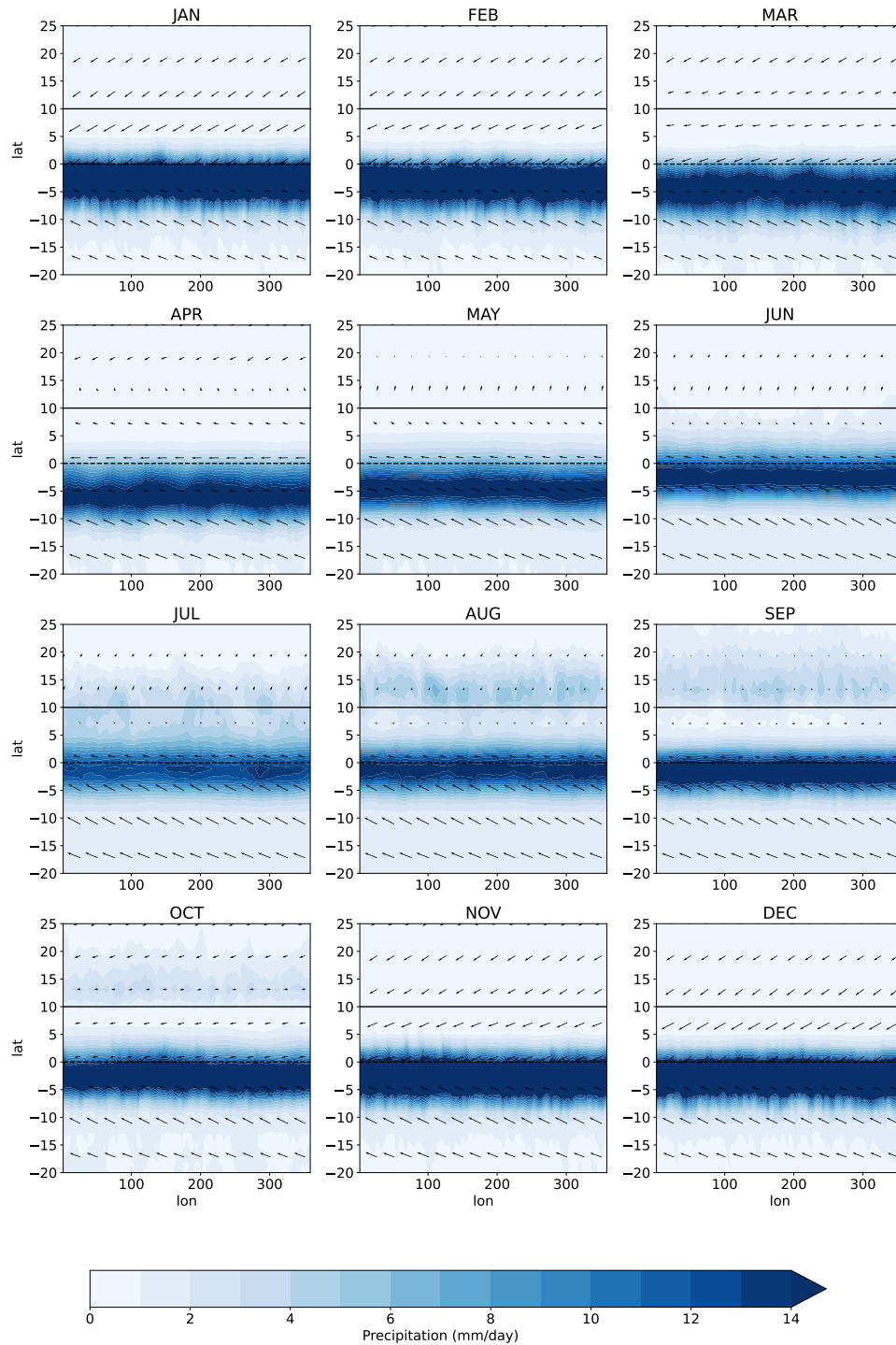


Figure S22: **Precipitation and surface wind direction for the Monsoon Planet throughout the year with slab ocean depth of 500m.** The continuous horizontal line marks the equator, the dashed horizontal line the location of land. The 20-years monthly averages are shown.

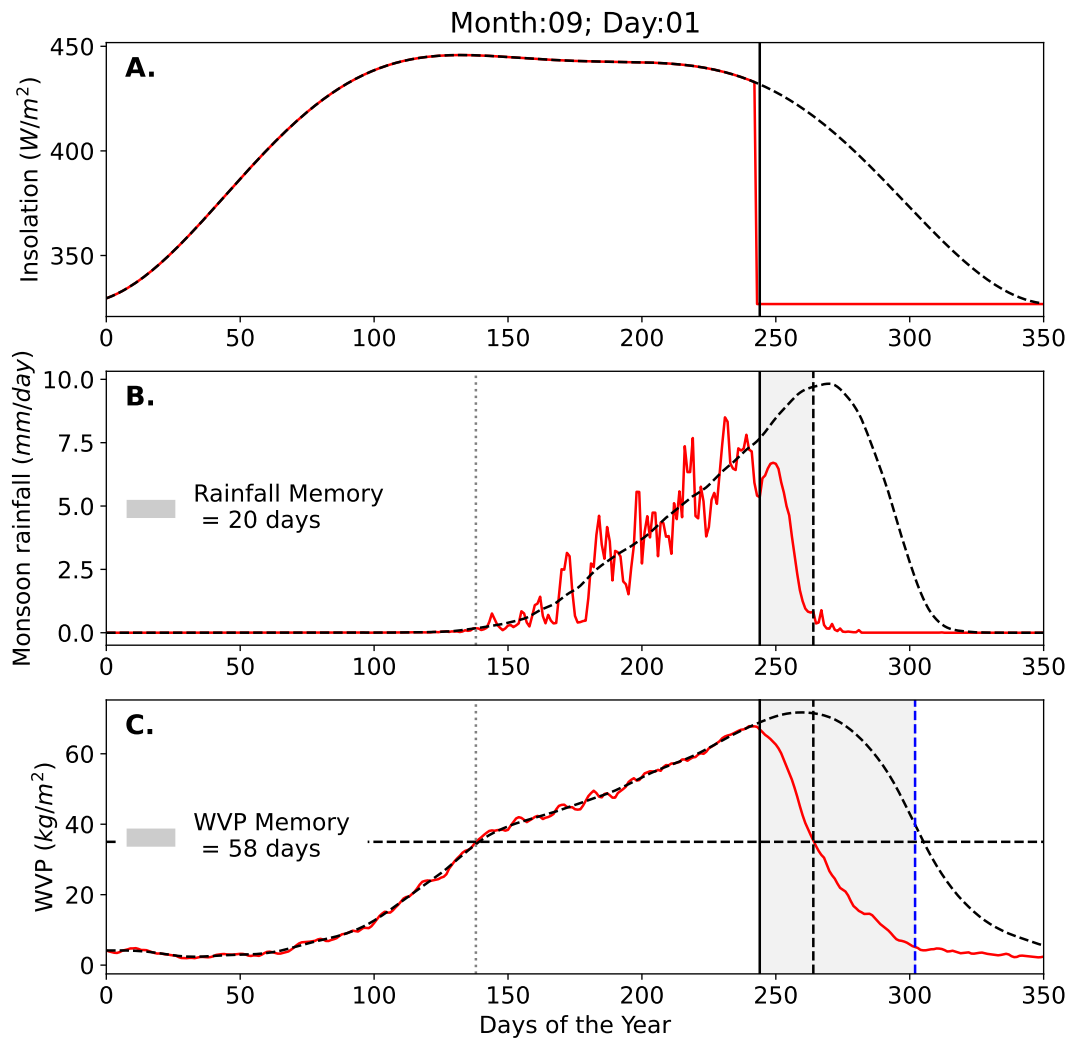


Figure S23: **Quantification of the memory effect for September 1st.** As in Fig. 3 but for September 1st.

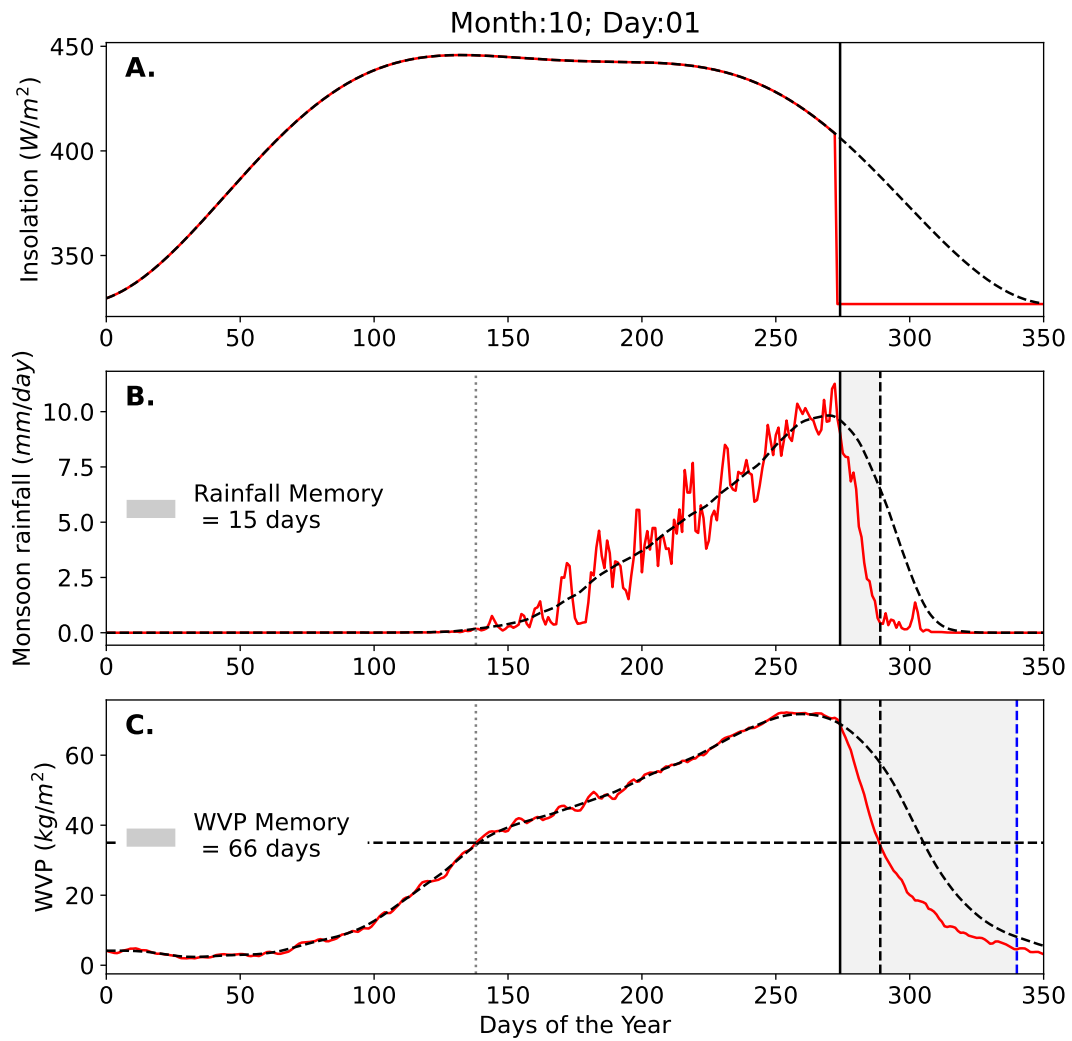


Figure S24: **Quantification of the memory effect for October 1st.** As in Fig. 3 but for October 1st.

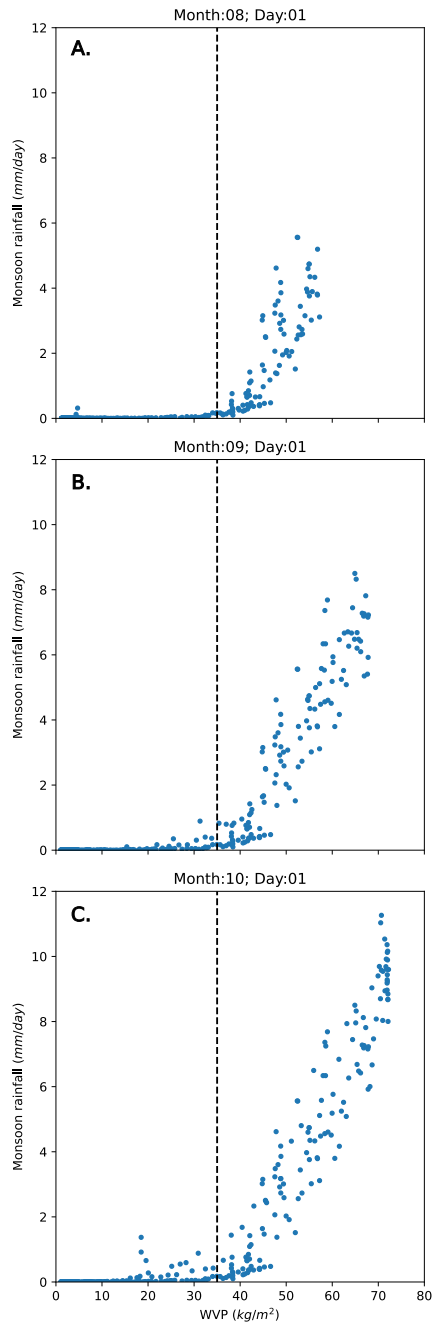


Figure S25: **Relationship between monsoon rainfall and water vapor (WVP).** Daily Monsoon Planet data for the monsoon region 10-20°N are shown. A water vapor level of approx. $35 kg/m^2$ (dashed vertical line) is needed for active monsoon rainfall. Plot is based on the 500 simulation days in Fig. 3, S23, S24.

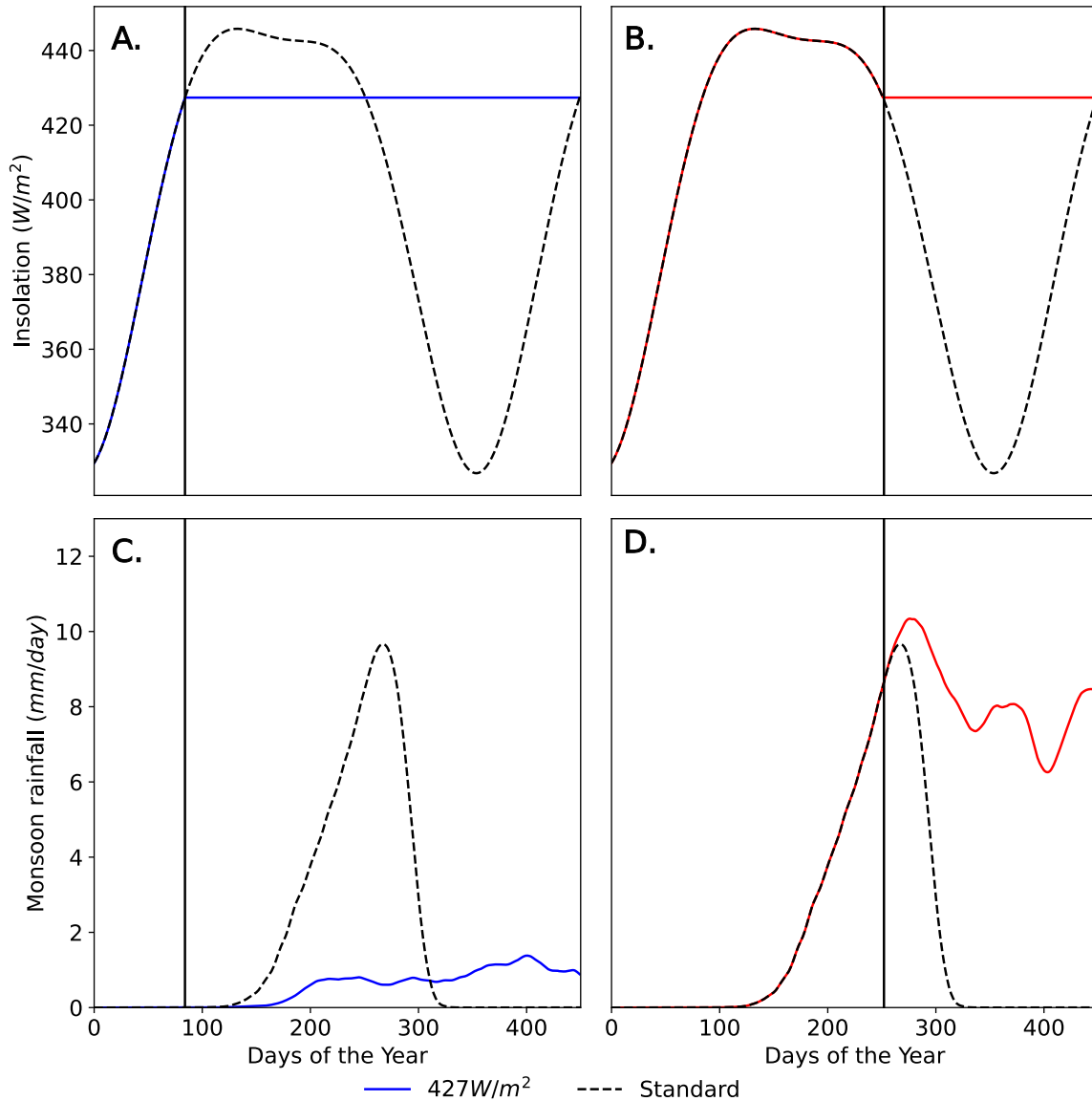


Figure S26: **Illustration of procedure.** Panel A and B show insolation in 10-20°N that runs naturally (dashed plot) until $427W/m^2$ which is reached on 25th March in spring (panel A) and 9th September in autumn (panel B). This time step is marked by the vertical black lines. Afterwards insolation is kept constant at $427W/m^2$ as shown in blue for spring and red for autumn. Panels C and D show precipitation without intervention (dashed) as well as intervened monsoon rainfall coming from the Off-State (blue) and coming from the On-State (red). One out of 5 ensemble members is presented. Daily data has been smoothed by singular spectrum analysis of window size 20.

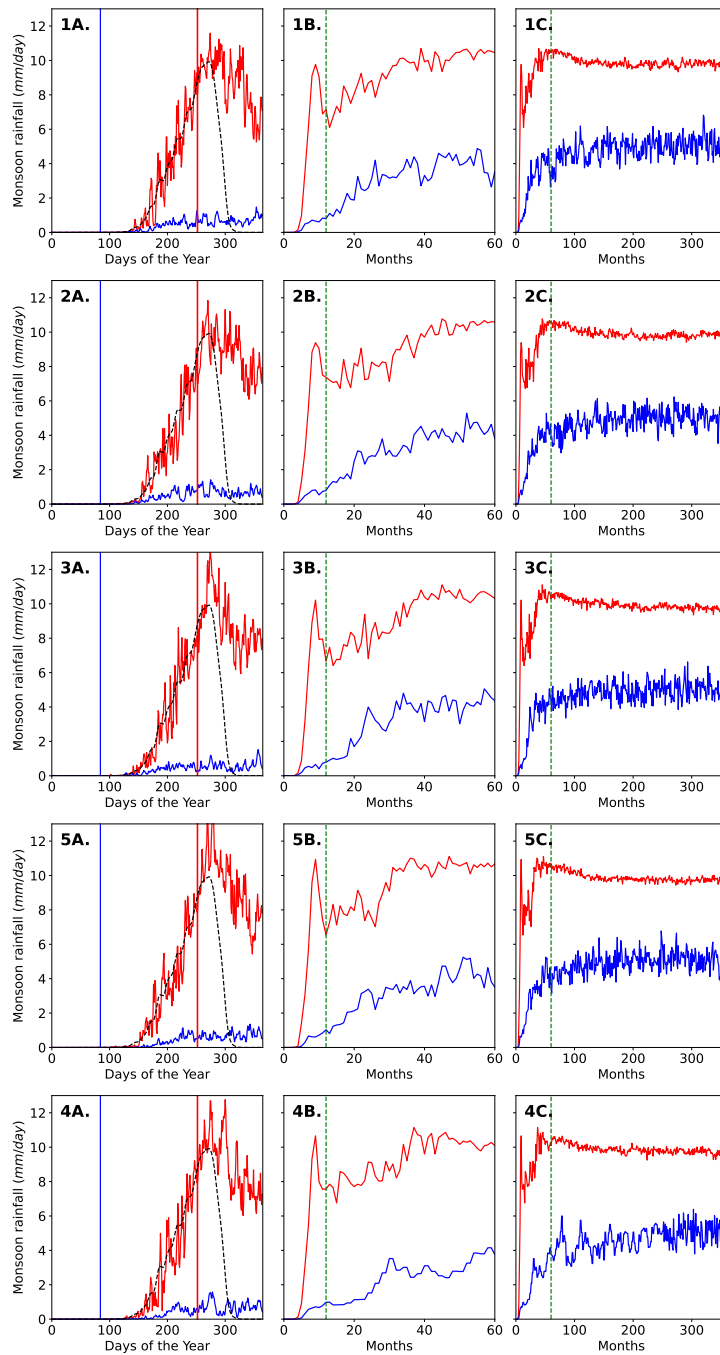


Figure S27: **Ensemble of two bistability simulations.** The ensemble of two simulations with varying initial conditions shows the same bistability behaviour underlying its robustness. Procedure and presentation as in Fig. 2B, but without any smoothing.

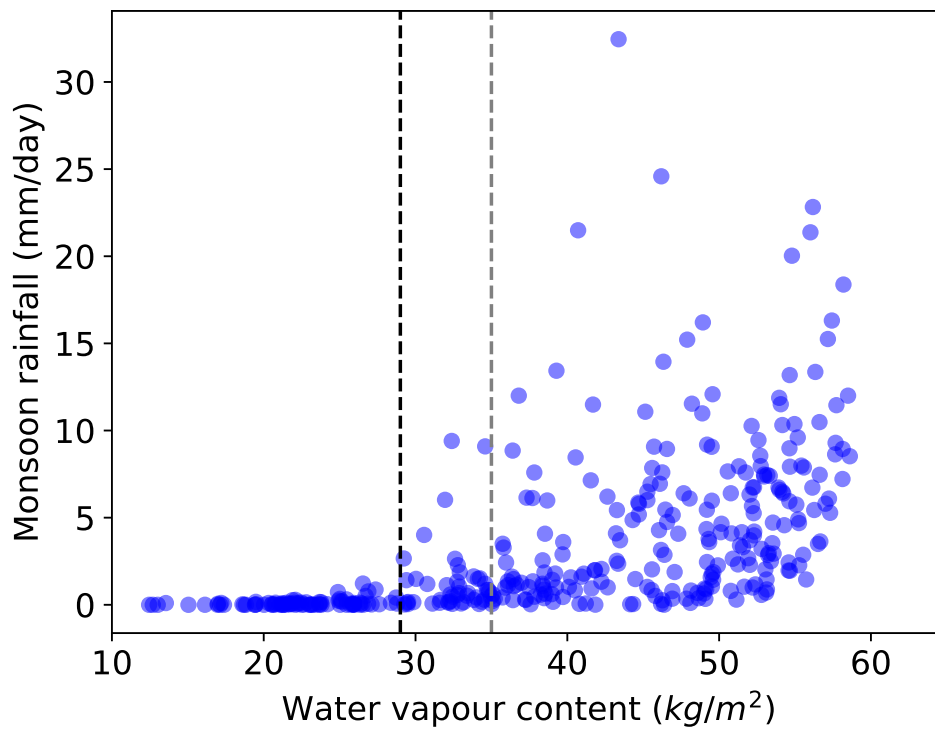


Figure S28: **Relationship between monsoon rainfall and water vapor content in reanalysis data.** In the reanalysis data, approx. 29 kg/m^2 of water vapour content are necessary for rainfall to occur, as marked with the black dashed line. The gray line marks the threshold as found in the Monsoon Planet setup. Data source: One year of daily ERA5 reanalysis data averaged over Central India ($10\text{-}20^\circ\text{N}$, $76\text{-}82^\circ\text{E}$).

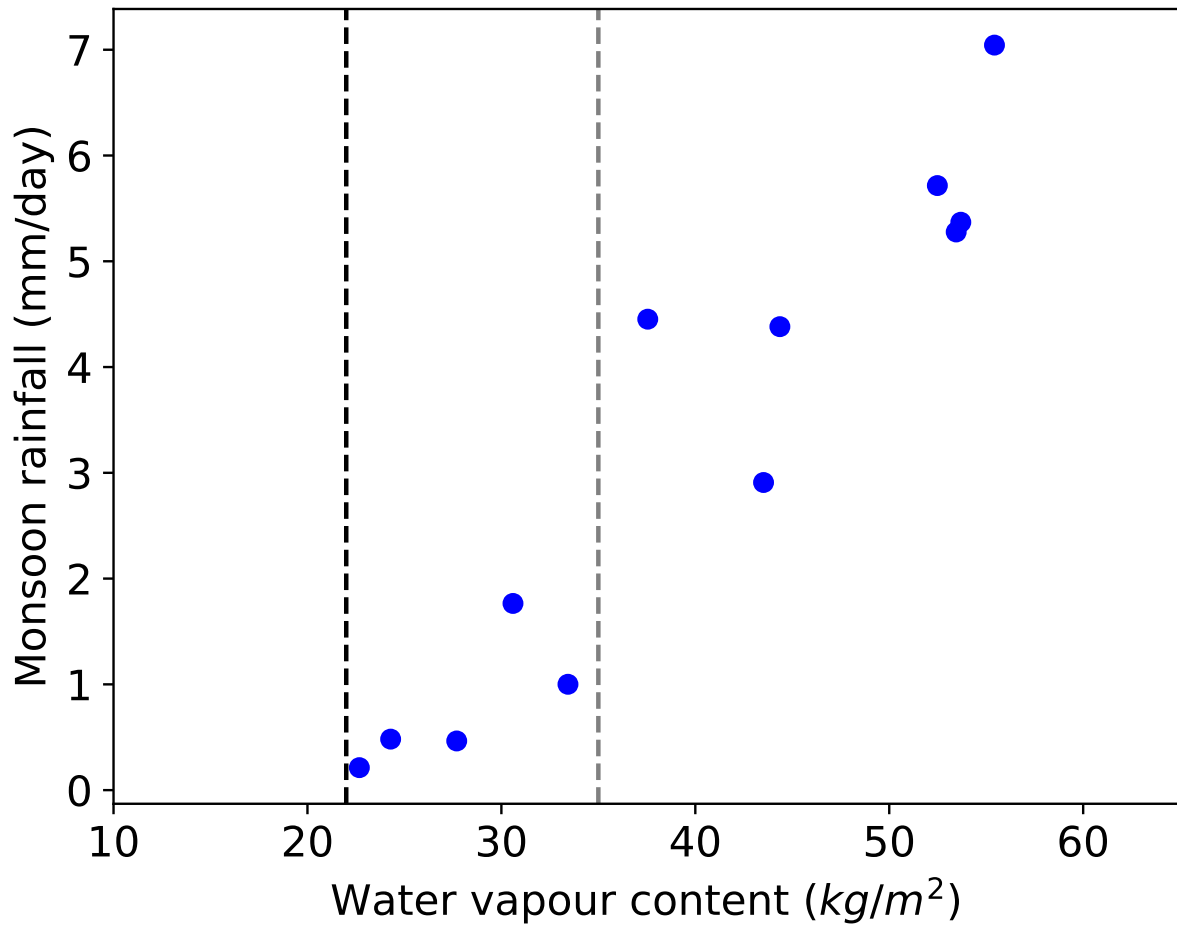


Figure S29: **Relationship between monsoon rainfall and water vapor content in reanalysis data.** As in Fig. S28, but for monthly averaged data over 10 years. Compare also to analysis in (I).

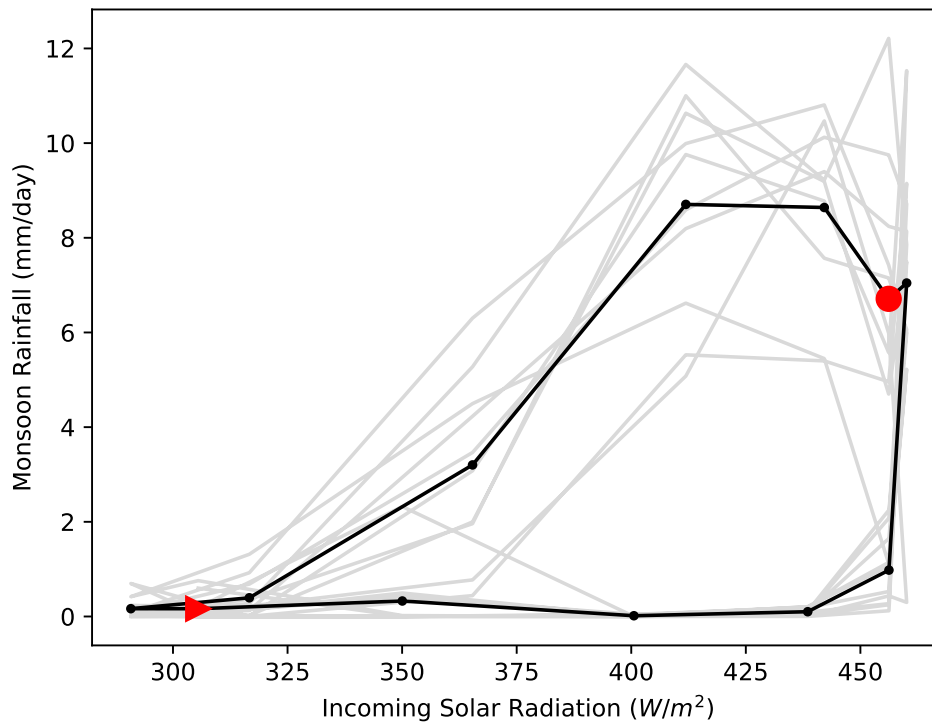


Figure S30: **Hysteresis in simulations with realistic topography and full ocean module.** The gray lines show 10 years of monthly data in gray, the monthly means are shown in black. The red triangle marks January and indicates the direction of progression of year, the red circle marks July. The hysteresis also sustains for this more realistic model setup.

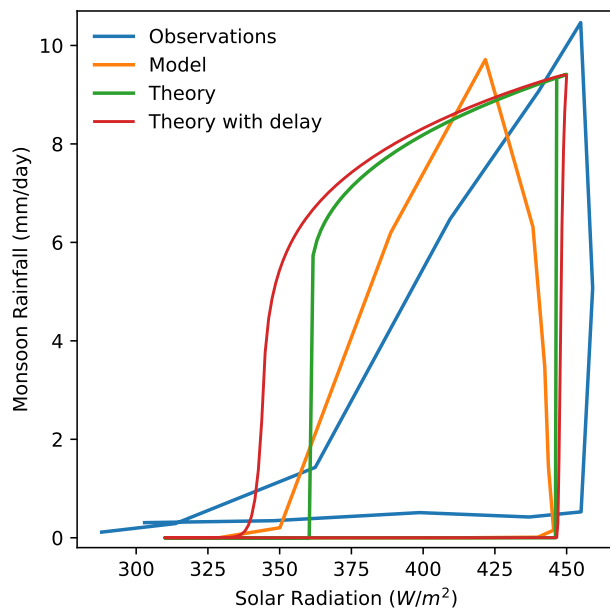


Figure S31: **Hysteresis based on minimalistic theory in comparison with model and observation based hysteresis.** As in Fig. 2 but including the hysteresis based on conceptual considerations as introduced in the SI.

Minimalistic model that shows seasonal monsoon hysteresis

Although the monsoon dynamics is obviously complex, the bistability and associated hysteresis behaviour can be reproduced in a very simple four equation model of the atmospheric column. To this end, we chose, out of the different equivalent formulations of atmospheric thermodynamics (entropy, moist static energy, enthalpy and the like), a potential energy- and moisture representation. The reason is that we adopt a large scale perspective of the atmospheric column. It has been shown that the release of latent heat from condensation of water vapor directly results in meso-scale eddy motion which is often capture in a term called turbulent kinetic energy (TKE) and not into large scale advective motion (2). The turbulent kinetic energy however is transported along the turbulent Richardson cascade into smaller and smaller scales and eventually into the molecular scale were it becomes heat.

Consider the energy balance of the atmospheric land column (with average temperature T_L) for a fixed temperature of the atmospheric column over ocean T_O , formulated in terms of the land-ocean temperature difference within the atmosphere $\Delta T = T_L - T_O$

$$HDLc_p \cdot \frac{dT_L}{dt} = HDLc_p \cdot \frac{d\Delta T}{dt} = DL \cdot R + DL \cdot \mathcal{L}P - HLc_p \cdot W \cdot \Delta T \quad (1)$$

where the right-hand side describes the temporal change in inner energy of the atmospheric column over land. H refers to the vertical extent of the lower troposphere, L and D to the horizontal scales of the region of precipitation. The constant c_p is the volumetric heat capacity of air at constant pressure and the constant \mathcal{L} is the latent heat of condensation. R denotes the net solar radiation into the atmospheric column, W the landward mean wind and P precipitation. Since it is assumed that the atmospheric temperature over the ocean is held constant by the large heat capacity of water, the temperature change over land is equal to $HDLc_p \cdot d\Delta T/dt$. The three terms on the right-hand side represent the net radiation contribution, the latent heat release and heat divergence.

The net radiation from the atmospheric land column is given by the solar insolation at the top of the atmosphere R_{sol} and the Stefan-Boltzmann law linearized around a base temperature T_B (temperature of the atmospheric column)

$$R = R_{sol} - R_{base} - 4\sigma T_B^3 \Delta T = R_s - \Gamma \Delta T \quad (2)$$

with the constant background heat radiation back to space $R_{base} = \sigma T_B^4$ and $R_s(t) \equiv R_{sol} - R_{base}$ which can be time dependent if the solar insolation is and the abbreviation $\Gamma \equiv 4\sigma T_{base}^3$. In the idealized model we choose

$$R_{sol} = R_{sol,base} + R_{sol,amp} \cdot \sin(R_{sol,freq} \cdot t) \quad (3)$$

We further assume ageostrophic monsoon winds proportional to the atmospheric temperature difference between land and ocean

$$W = \alpha \Delta T \quad (4)$$

The qualitative behaviour of the conceptual model is already captured using the assumption of instantaneous adjustment of winds to the temperature difference. Alternatively one can assume an adjustment over a period τ_W and replace the diagnostic equation (4) by a prognostic equation for the winds:

$$\frac{dW}{dt} = \frac{\alpha \Delta T - W}{\tau_W} \quad (5)$$

This equation was used with a parameter $\tau_W = 2$ days to obtain the red curve in Fig. S31.

The moisture balance of the atmospheric land column is

$$HDL\rho_A \frac{dq_L}{dt} = HL\rho_A \cdot W \cdot (q_O - q_L) - DL \cdot P \quad (6)$$

with the mean air density ρ_A , and the specific humidity over land and ocean q_L and q_O .

The rainfall is assumed to be proportional to the atmospheric moisture content over land

$$P = \beta q_L \quad (7)$$

Alternatively one can also assume an adjustment over a period τ_P and replace the diagnostic equation (7) by a prognostic equation for the precipitation:

$$\frac{dP}{dt} = \frac{\beta q_L - P}{\tau_P} \quad (8)$$

This equation was used with a parameter $\tau_P = 1$ hour to obtain the red curve in Fig. S31. The specific implemented values can be found in Table 1.

For convenience define the constants

$$\Delta T_O \equiv \frac{D\beta}{H\rho_A\alpha}, \quad (9)$$

$$R_O \equiv \Gamma \cdot \Delta T_O, \quad (10)$$

$$P_O \equiv \beta \cdot q_O, \quad (11)$$

and

$$R_b \equiv \frac{c_p\beta^2}{\epsilon\rho_A^2\alpha} \quad (12)$$

This allows an easy transformation between a temperature- and a precipitation formulation of the equilibrium problem (as defined by setting all time derivatives to zero), via

$$P = \frac{\Delta T}{\Delta T + \Delta T_O} \cdot P_O \quad (13)$$

The two transition points of the hysteresis can be approximated from the steady state equations, i.e. by setting equations (1) and (6) to zero, since the equilibration times for these equations are much faster than the change in the solar forcing. Combining the above relations yields the governing equations

$$A\Delta T^3 + (A\Delta T_O + \Gamma)\Delta T^2 + (\Gamma\Delta T_O - \mathcal{L}P_O - R_s)\Delta T - R_s\Delta T_O = 0 \quad (14)$$

with the abbreviation $A \equiv \alpha \cdot H/D$. The right transition point, denoted as R_\wedge , is reached when the temperature difference transitions into negative values, i.e. at $\Delta T = 0$, which means that

$R_s = 0$ and thus,

$$R_{sol} = R_{base} \quad (15)$$

The left transition point is given as the critical point of the relation $R(\Delta T)$ as defined intrinsically by equation (16). Alternatively it can be derived from the P-formulation of the problem in equation (17).

This conceptual model shows the same hysteresis behaviour as the observations and numerical model results (green curve in Fig. S31). These equations complement an earlier equilibrium consideration (3) with the atmospheric long-wave radiations feedback. Allowing for inertia in the dynamic adjustment between the temperature difference and the winds as well as for a possible thermodynamic inertia between moisture accumulation and condensation, yields a slightly smoother transition towards the off-state as is found in observations and the atmospheric general circulation model (red curve in Fig. S31)

The essence of the moisture-advection feedback is captured in this model. In order to account for potential temporal processes for the wind to adjust to a changing temperature difference or the precipitation emerging from a given atmospheric moisture content, equations (4) and (7) can be replaced by equations (5) and (8) with adjustment time scales τ_W and τ_P , respectively. The python scripts for both models with and without time delay are available at <https://github.com/ALevermann/MonsoonHysteresis>.

Combining the energy- and the moisture balance of the atmospheric land column with the assumption that the monsoon winds are proportional to the temperature difference between atmospheric land and ocean columns and that the precipitation is proportional to the atmospheric moisture, yields a cubic polynomial in the precipitation P as a function of the solar insolation R for the non-dimensionalized precipitation p .

Variable	Value/Description
c_p	$1,295 \text{ Jm}^{-3} \text{ K}^{-1}$
H	15,000 m
D	2,725 m
\mathcal{L}	$2.6 \times 10^6 \text{ Jkg}^{-1}$
α	$0.6 \text{ ms}^{-1} \text{ K}^{-1}$
β	$0.8 \times \left(\frac{24 \cdot 60 \cdot 60}{1,000,000} \right) \text{ kg m}^{-2} \text{ s}^{-1}$
ρ_A	$1.24 \times 10^{-3} \text{ kg m}^{-3}$
q_O	$5.1 \times 10^{-3} \text{ kg kg}^{-1}$
P_O	$\beta \times q_O \text{ kg m}^{-2} \text{ s}^{-1}$
T_O	5 K above T_{base}
$R_{\text{sol,base}}$	380 W m^{-2}
$R_{\text{sol,amp}}$	70 W m^{-2}
$R_{\text{sol,freq}}$	$2\pi / (365 \cdot 24 \cdot 60 \cdot 60 \text{ s})$
R_{sol}	$R_{\text{sol,base}} + R_{\text{sol,amp}} \sin(R_{\text{sol,freq}} t)$
σ	$5.670374419 \times 10^{-8} \text{ W m}^{-2} \text{ K}^{-4}$
T_{base}	293 K
Γ	$4\sigma T_{\text{base}}^3$
$R_{\text{out,base}}$	σT_{base}^4
R_{out}	$R_{\text{out,base}} + \Gamma T_O$
τ_W	2 days
τ_P	1 hour

Table 1: Overview of implemented values

$$p^3 + p^2 - (\gamma \cdot r - l)p + r = 0 \quad (16)$$

$$(\mathcal{L}P + R_s) \cdot (P_O - P)^2 = R_O P \cdot (P_O - P) + R_b \cdot P^2, \quad \forall P < P_O \quad (17)$$

with parameters R_O , R_b and P_O and the latent heat of condensation $\mathcal{L} = 2.6 \cdot 10^6 \text{ J/kg}$. R denotes the net solar radiation into the atmospheric column which is negative in monsoon regions (See Fig. 2 in (3) for observations, Fig. 5 in (4) for the Monsoon Planet). If monsoon systems around the world follow this kind of dynamics they would be so-called tipping elements of the climate system, both in the original quantitative definition of the word (5) and under the

dynamical definition (6) that has been adapted more recently on a broader scale (7).

Other Supplementary Material

The upper and lower panel of Fig. S15 are individually available as dynamic gifs with vary upper (solar radiation) and lower boundary conditions (surface temperature). For specific boundary conditions, the different rainfall regimes and associated dates are shown. Fig. S17 is available as interactive version, see Data Availability Statement.

References

1. Mallesh, Rakshith and Srinivasan, Jayaraman, How is the relationship between rainfall and water vapor in the Indian monsoon influenced by changes in lapse rate during global warming?, *Environmental Research Communications*, 2024, DOI: 10.1088/2515-7620/ad2c64.
2. Emanuel, Kerry A and David Neelin, J and Bretherton, Christopher S, On large-scale circulations in convecting atmospheres, *Quarterly Journal of the Royal Meteorological Society*, 120, 1111–1143, 1994, DOI: 10.1002/qj.49712051902.
3. Levermann, Anders and Schewe, Jacob and Petoukhov, Vladimir and Held, Hermann, Basic mechanism for abrupt monsoon transitions, *Proceedings of the National Academy of Sciences*, 106, 20572–20577, 2009, DOI: 10.1073/pnas.0901414106.
4. Katzenberger, Anja and Petri, Stefan and Feulner, Georg and Levermann, Anders, Monsoon Planet: Bimodal Rainfall Distribution due to Barrier Structure in Pressure Fields, *Journal of Climate*, 37, 1295–1315, 2024, DOI: 10.1175/JCLI-D-23-0055.1.
5. Timothy M. Lenton and Hermann Held and Elmar Kriegler and Jim W. Hall and Wolfgang Lucht and Stefan Rahmstorf and Hans Joachim Schellnhuber, Tipping elements in the Earth's

climate system, *Proceedings of the National Academy of Sciences*, 105, 1786-1793, 2008, DOI: 10.1073/pnas.0705414105.

6. Levermann, Anders and Bamber, Jonathan and Drijfhout, Sybren and Ganopolski, Andrey and Haeberli, Winfried and Harris, Neil and Huss, Matthias and Krueger, Kirstin and Lenton, Timothy and Lindsay, Ronald and Notz, Dirk and Wadhams, Peter and Weber, Susanne, Potential climatic transitions with profound impact on Europe, *Climatic Change*, 110,
7. David I. Armstrong McKay and Arie Staal and Jesse F. Abrams and Ricarda Winkelmann and Boris Sakschewski and Sina Loriani and Ingo Fetzer and Sarah E. Cornell and Johan Rockström and Timothy M. Lenton, Exceeding 1.5°C global warming could trigger multiple climate tipping points, *Science*, 377, eabn7950, 2022, DOI: 10.1126/science.abn7950.